

2

Supercontinuum Generation in Condensed Matter

Q.Z. WANG, P.P. HO, and R.R. ALFANO

1. Introduction

Supercontinuum generation, the production of intense ultrafast broadband “white light” pulses, arises from the propagation of intense picosecond or shorter laser pulses through condensed or gaseous media. Various processes are responsible for continuum generation. These are called self-, induced-, and cross-phase modulations and four-photon parametric generation. Whenever an intense laser pulse propagates through a medium, it changes the refractive index, which in turn changes the phase, amplitude, and frequency of the incident laser pulse. A phase change can cause a frequency sweep within the pulse envelope. This process has been called *self-phase modulation (SPM)* (Alfano and Shapiro, 1970a). Nondegenerate *four-photon parametric generation (FPPG)* usually occurs simultaneously with the SPM process (Alfano and Shapiro, 1970a). Photons at the laser frequency parametrically generate photons to be emitted at Stokes and anti-Stokes frequencies in an angular pattern due to the required phase-matching condition. When a coherent vibrational mode is excited by a laser, stimulated Raman scattering (SRS) occurs. SRS is an important process that competes and couples with SPM. The interference between SRS and SPM causes a change in the emission spectrum resulting in *stimulated Raman scattering cross-phase modulation (SRS-XPM)* (Gersten et al., 1980). A process similar to SRS-XPM occurs when an intense laser pulse propagates through a medium possessing a large second-order χ^2 and third-order χ^3 susceptibility. Both second harmonic generation (SHG) and SPM occur and can be coupled together. The interference between SHG and SPM alters the emission spectrum and is called *second harmonic generation cross-phase modulation (SHG-XPM)* (Alfano et al., 1987). A process closely related to XPM, called *induced phase modulation (IPM)* (Alfano, 1986), occurs when a weak pulse at a different frequency propagates through a disrupted medium whose index of refraction is changed by an intense laser pulse. The phase of the weak optical field can be modulated by the time variation of the index of refraction originating from the primary intense pulse.

TABLE 2.1. Brief history of experimental continuum generation.

Investigator	Year	Material	Laser wavelength/ pulsewidth	Spectrum	Frequency (cm ⁻¹)	Process
Alfano, Shapiro	1968–1973	Liquids and solids	530 nm/ 8 ps or 1060 nm/ 8 ps	Visible and near IR	6,000	SPM
Stolen et al.	1974–1976	Fibers	530 nm/ns	Visible	500	SPM
Shank, Fork et al.	1983	Glycerol	620 nm/100 fs	UV, visible, near IR	10,000	SPM
Corkum, Ho, Alfano	1985	Semiconductors dielectrics	10 μ m/6 ps	IR	1,000	SPM
Corkum, Sorokin	1986	Gases	600 nm/2 ps 300 nm/0.5 ps	Visible and UV	5,000	SPM
Alfano, Ho, Manassah, Jimbo	1986	Glass	1,060 nm/ 530 nm/8 ps	Visible	1,000	IPM (XPM)
Alfano, Ho, Wang, Jimbo	1986	ZnSe	1,060 nm/8 ps	Visible	1,000	SHG-XPM (ISB)
Alfano, Ho, Baldeck	1987	Fibers	530 nm/30 ps	Visible	1,000	SRS-XPM

The first study of the generation and mechanisms of the ultrafast supercontinuum dates back to the years 1968 to 1972, when Alfano and Shapiro first observed the “white” picosecond continuum in liquids and solids (Alfano and Shapiro, 1970a). Spectra extending over $\sim 6000\text{cm}^{-1}$ in the visible and infrared wavelength region were observed. Over the years, improvements in the generation of ultrashort pulses from mode-locked lasers led to the production of wider supercontinua in the visible, ultraviolet, and infrared wavelength regions using various materials. Table 2.1 highlights the major accomplishments in this field over the past 20 years.

In this chapter we focus on the picosecond supercontinuum generation in liquids, solids, and crystals. Supercontinuum generation in gases, XPM, and IPM are discussed by Corkum and Rolland (Chapter 7), Glowina et al. (Chapter 8), Baldeck et al. (Chapter 4), Agrawal (Chapter 3), and Manassah (Chapter 5), respectively.

2. Simplified Model

Before we go further, let us first examine the nonlinear wave equation to describe the self-phase modulation mechanism. A thorough theoretical study of supercontinuum generation has been dealt with in Chapters 1, 3, and 5.

The optical electromagnetic field of a supercontinuum pulse satisfies Maxwell's equations:

$$\begin{aligned}\nabla \times \mathbf{E} &= -\frac{1}{c} \frac{\partial \mathbf{B}}{\partial t}, \\ \nabla \times \mathbf{H} &= \frac{1}{c} \frac{\partial \mathbf{D}}{\partial t} + \frac{4\pi}{c} \mathbf{J}, \\ \nabla \cdot \mathbf{D} &= 4\pi\rho, \\ \nabla \cdot \mathbf{B} &= 0.\end{aligned}\tag{1}$$

Equations (1) can be reduced to (see Appendix)

$$\frac{\partial A}{\partial z} + \frac{1}{v_g} \frac{\partial A}{\partial t} = i \frac{\omega_0 n_2}{2c} |A|^2 A,\tag{2}$$

where $A(z, t)$ is the complex envelope of the electric field and $v_g = 1/(\partial k/\partial \omega)_{\omega_0}$ is the group velocity. The total refractive index n is defined by $n^2 = n_0^2 + 2n_0 n_2 |A(t)|^2$, where n_2 is the key parameter called the nonlinear refractive index. This coefficient is responsible for a host of nonlinear effects: self- and cross-phase modulation, self-focusing, and the optical Kerr effect, to name the important effects. Equation (2) was derived using the following approximations: (1) linearly polarized electric field, (2) homogeneous radial fields, (3) slowly varying envelope, (4) isotropic and nonmagnetic medium, (5) negligible Raman effect, (6) frequency-independent nonlinear susceptibility $\chi^{(3)}$, and (7) neglect of group velocity dispersion, absorption, self-steepening, and self-frequency shift.

Denoting by a and α the amplitude and phase of the electric field envelope $A = ae^{i\alpha}$, Eq. (2) reduces to

$$\frac{\partial a}{\partial z} + \frac{1}{v_g} \frac{\partial a}{\partial t} = 0\tag{3a}$$

and

$$\frac{\partial \alpha}{\partial z} + \frac{1}{v_g} \frac{\partial \alpha}{\partial t} = \frac{\omega_0 n_2}{2c} a^2.\tag{3b}$$

The analytical solutions for the amplitude and phase are

$$a(\tau) = a_0 F(\tau)\tag{4a}$$

and

$$\alpha(z, \tau) = \frac{\omega_0 n_2}{2c} \int_0^z a^2 dz' = \frac{\omega_0 n_2}{2c} a_0^2 F^2(\tau) z,\tag{4b}$$

where a_0 is the amplitude, $F(\tau)$ the pulse envelope, and τ the local time $\tau = t - z/v_g$. For materials whose response time is slower than pure electronic but faster than molecular orientation (i.e., coupled electronic, molecular

redistribution, libratory motion) the envelope is just the optical pulse shape. For a “pure” electronic response, the envelope should also include the optical cycles in the pulse shape.

The electric field envelope solution of Eq. (2) is given by

$$A(z, \tau) = a(\tau) \exp \left[i \frac{\omega_0 n_2}{2c} a_0^2 F^2(\tau) z \right]. \quad (5)$$

The main physics behind the supercontinuum generation by self-phase modulation is contained in Eq. (5) and is displayed in Figure 2.1. As shown in Figure 2.1a, the index change becomes time dependent and, therefore, the phase of a pulse propagating in a distorted medium becomes time dependent, resulting in self-phase modulation. The electric field frequency is continuously shifted (Figure 2.1c) in time. This process is most important in the generation of femtosecond pulses (see Chapter 10 by Johnson and Shank).

Since the pulse duration is much larger than the optical period $2\pi/\omega_0$ (slowly varying approximation), the electric field at each position τ within the

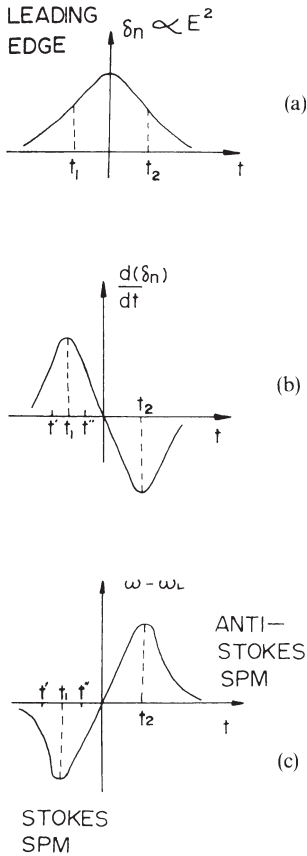


FIGURE 2.1. A simple mechanism for SPM for a non-linear index following the envelope of a symmetrical laser pulse: (a) time-dependent nonlinear index change; (b) time rate of change of index change; (c) time distribution of SPM-shifted frequencies $\omega(t) - \omega_0$.

pulse has a specific *local* and *instantaneous frequency* at given time that is given by

$$\omega(\tau) = \omega_0 + \delta\omega(\tau), \quad (6a)$$

where

$$\delta\omega(\tau) = -\frac{\partial\alpha}{\partial\tau} = -\frac{\omega_0}{2c} n_2 a_0^2 z \frac{\partial F^2(\tau)}{\partial\tau}. \quad (6b)$$

The $\delta\omega(\tau)$ is the frequency shift generated at a particular time location τ within the pulse shape. This frequency shift is proportional to the derivative of the pulse envelope, which corresponds to the generation of new frequencies resulting in wider spectra.

Pulses shorter than the excitation pulse can be produced at given frequencies. It was suggested by Y.R. Shen many years ago that Alfano and Shapiro in 1970 most likely produced femtosecond pulses via supercontinuum generation. Figure 2.1c shows the frequency distribution within the pulse shape. The leading edge, the pulse peak, and the trailing edge are red shifted, non-shifted, and blue shifted, respectively.

The spectrum of SPM pulses is obtained by taking the Fourier transform of the complex temporal envelope $A(z, \tau)$:

$$A(\Omega) = \frac{1}{2\pi} \int_{-\infty}^{\infty} A(z, \tau) \exp[i\Omega\tau] d\tau, \quad (7)$$

where $\Omega = \omega - \omega_0$. The intensity spectrum is given by

$$S(\Omega, z) = \frac{c}{4\pi} |A(\Omega, z)|^2. \quad (8)$$

In practical cases, the phase of $A(z, \tau)$ is large compare with π , and the stationary phase method leads to

$$\Delta\omega(z)_{\max} = \frac{\omega_0}{2c} n_2 a_0^2 \left[\left. \frac{\partial F^2}{\partial\tau} \right|_{\tau_1} - \left. \frac{\partial F^2}{\partial\tau} \right|_{\tau_2} \right] z. \quad (9)$$

The intensity

$$\begin{aligned} S(\Omega, z) = & \left(\frac{c}{4\pi} \right) \left(\frac{4\pi c}{\omega_0 n_2 z} \right) \left\{ F^2(\tau') \left/ \frac{\partial F^2}{\partial\tau^2} \right|_{\tau'} + F^2(\tau'') \left/ \frac{\partial^2 F^2}{\partial\tau^2} \right|_{\tau''} \right. \\ & + 2 \frac{F(\tau') F(\tau'')}{\left[\partial^2 F^2 / \partial\tau^2 \right|_{\tau'} \partial^2 F^2 / \partial\tau^2 \big|_{\tau''}]^{1/2}} \\ & \left. \times \cos \left[\Omega(\tau' - \tau'') + \frac{\omega_0}{2c} n_2 a_0^2 z (F^2(\tau') - F^2(\tau'')) \right] \right\}, \end{aligned} \quad (10)$$

where $\Delta\omega_{\max}$ is the maximum frequency spread, τ_1 and τ_2 are the pulse envelope inflection points, and τ' and τ'' are the points of the pulse shape that have the same frequency.

An estimate of the modulation frequency $\delta\omega_M$ can be made by calculating the maximum number of interference minima and dividing this number into the maximum frequency broadening. A straightforward calculation leads to

$$\delta\omega_M \approx 2\pi \left. \frac{\partial F^2}{\partial \tau} \right|_{\tau_1} / F^2(\tau_1) \approx 2\pi \left. \frac{\partial F^2}{\partial \tau} \right|_{\tau_2} / F^2(\tau_2). \quad (11)$$

For a Gaussian laser pulse given by

$$F(\tau) = \exp[-\tau^2/2\tau_0^2], \quad (12)$$

the modulation frequency of the SPM spectrum is (Alfano, 1972)

$$\delta\omega_M = \frac{4\pi}{\tau_0} \quad \text{or} \quad \delta\bar{\nu}_M = \frac{2}{\tau_0 c}. \quad (13)$$

Using this relation, the average modulation period of 13 cm^{-1} corresponds to an initial pulse duration of 5 ps emitted from mode-locked Nd:glass laser. The maximum frequency extent in this case is (Alfano, 1972)

$$\Delta\omega_{\max} \approx \frac{\omega_0 n_2 a_0^2 z}{c \tau_0}. \quad (14)$$

The maximum frequency shift (Eq. (14)) indicates the following salient points:

- The frequency extent is inversely proportional to the pumping pulse duration. The shorter the incoming pulse, the greater the frequency extent. The first white light band supercontinuum pulses were generated using picosecond laser pulses (Alfano and Shapiro, 1970a,b).
- The spectral broadening is proportional to n_2 . The supercontinuum generation can be enhanced by increasing the nonlinear refractive index. This is discussed in detail in Section 6.
- The spectral broadening is linearly proportional to amplitude a_0^2 . Therefore, multiple-excitation laser beams of different wavelengths may be used to increase the supercontinuum generation. This leads to the basic principle behind IPM and XPM. These processes are described by Baldeck et al. (Chapter 4) and Manassah (Chapter 5).
- The spectral broadening is proportional to ω_0 and z .

The chirp—the temporal distribution of frequency in the pulse shape—is an important characteristic of SPM broadened pulse. In the linear chirp approximation, the chirp coefficient C is usually defined by the phase relation

$$\alpha = C\tau^2. \quad (15)$$

For a Gaussian electric field envelope and linear approximation, the envelope reduces to

$$F^2(\tau) = \exp[-\tau^2/\tau_0^2] \approx 1 - \tau^2/\tau_0^2. \quad (16)$$

The linear chirp coefficient derived from Eqs. (5) and (16) becomes

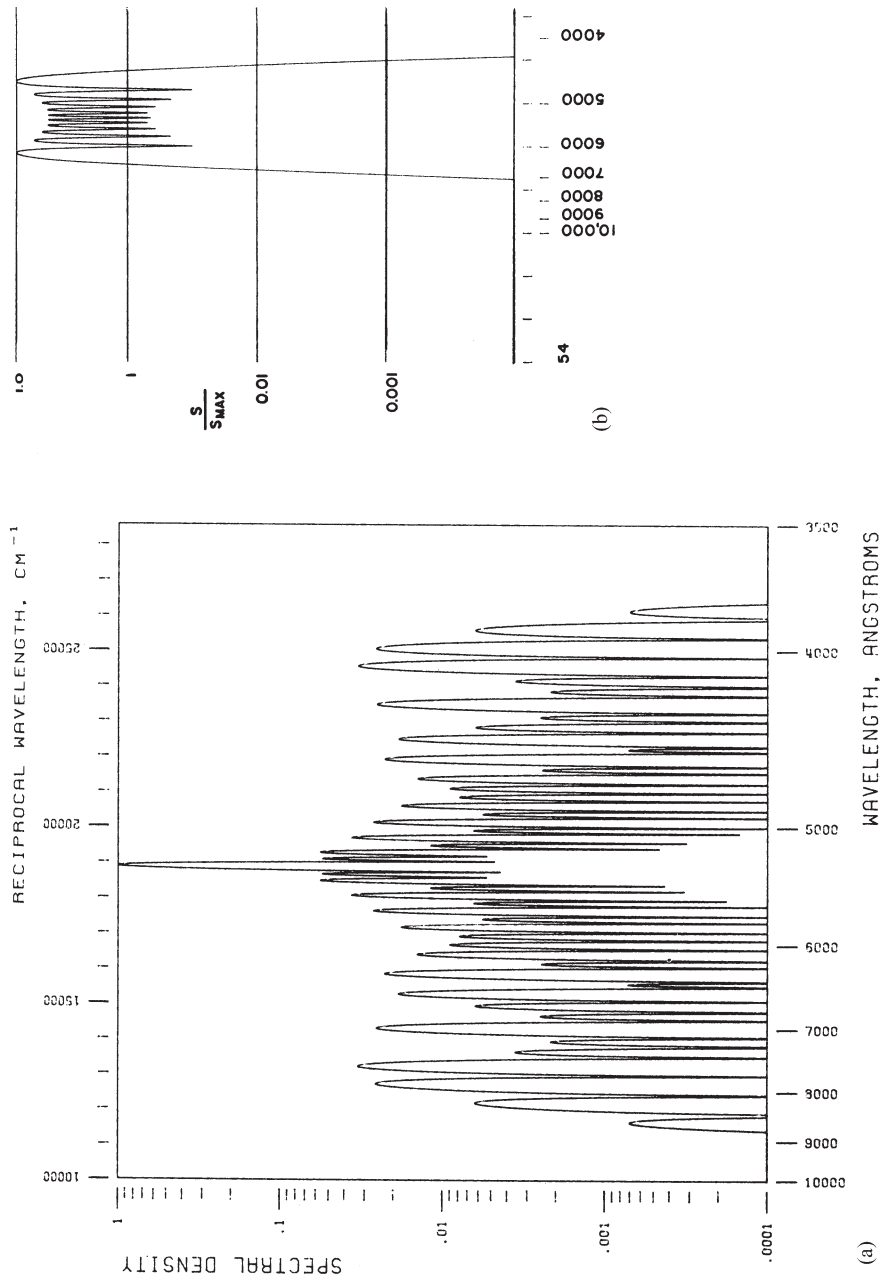


FIGURE 2.2. Calculated SPM spectrum: (a) for response time slower than pure electronic but faster than molecular orientation: $\beta = 30$ and $\tau = 0.1$ ps; (b) for pure electronic response: $\beta = 30$ and $\tau = 0.1$ ps. (From Alfano, 1972.)

$$C = \left(\frac{\omega_0}{2c} \right) \left(\frac{n_2 a_0^2 z}{\tau_0^2} \right). \quad (17)$$

Typical calculated SPM spectra are displayed in Figure 2.2. The spectral densities of the SPM light are normalized and β is defined as $\beta = (n_2 a_0^2 \omega_0 z)/2c$, which measures the strength of the broadening process. Figure 2.2a shows the spectrum for a material response time slower than pure electronic but faster than molecular orientation for $\beta = 30$ and $\tau = 0.1$ ps. The extent of the spectrum is about 7000 cm^{-1} . Figure 2.2b shows the SPM spectrum for a quasi-pure electronic response for $\beta = 30$ and $\tau = 0.1$ ps. Typical SPM spectral characteristics are apparent in these spectra.

3. Experimental Arrangement for SPM Generation

To produce the supercontinuum, an ultrafast laser pulse is essential with a pulse duration in the picosecond and femtosecond time region. A mode-locked laser is used to generate picosecond and femtosecond light pulses. Table 2.2 lists the available mode-locked lasers that can produce picosecond and femtosecond laser pulses. Measurements performed in the 1970s used a modelocked Nd:glass laser with output at $1.06 \mu\text{m}$ with power of $\sim 5 \times 10^9 \text{ W}$ and the second harmonic (SHG) at 530 nm with power of $2 \times 10^8 \text{ W}$. Typically, one needs at least a few microjoules of 100-fs pulse passing through a 1-mm sample to produce continuum.

A typical experimental setup for ultrafast supercontinuum generation is shown in Figure 2.3. Both spectral and spatial distributions are measured. The 8-ps SHG pulse of 5 mJ is reduced in size to a collimated 1.2-mm-diameter beam across the sample by an inverted telescope. For weaker excitation pulses, the beam is focused into the sample using a 10- to 25-cm focal lens. The typical sample length used is 10 to 15 cm for picosecond pulses and 0.1 to 1 cm for 100-f pulses. The intensity distribution of the light at the exit face of the sample was magnified 10 times and imaged on the slit of a spec-

TABLE 2.2. Available ultrafast mode-locked lasers.

Oscillator	Wavelength (nm)	Pulse duration
Ruby	694.3	30 ps
YAG	1064	30 ps
Silicate glass	1060	8 ps
Phosphate glass	1054	6 ps
Dye	Tunable (SYNC or flash lamp)	5–10 ps
Dye + CO ₂ + semiconductor switches	9300	1–10 ps
Dye (CPM)	610–630	100 fs
Dye + pulse compression (SYNC)	Tunable	300 fs
Dye + CPM (prisms in cavity)	620	27–60 fs
Dye + SPM + pulse compression (prisms and grating pairs)	620	6–10 fs

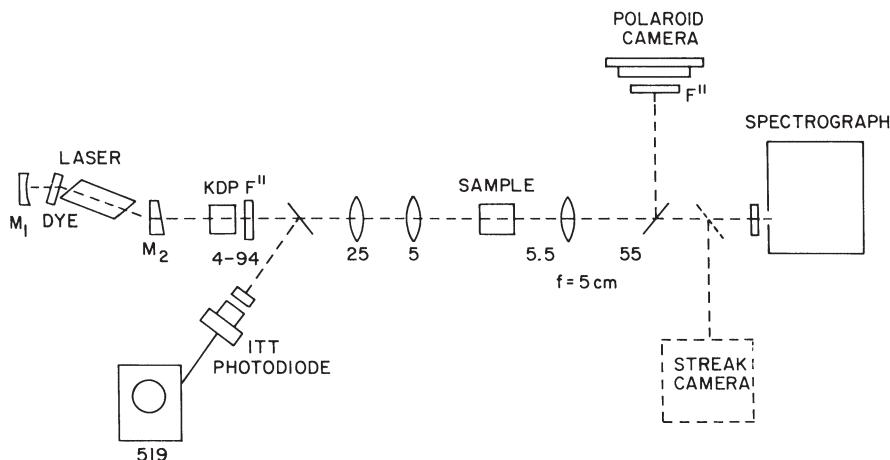


FIGURE 2.3. Experimental arrangement for generating and observing supercontinuum and self-focusing. (From Alfano, 1972.)

trograph. The spectrum of each individual filament within the slit was displayed. Usually there were 5 to 20 filaments. A thin quartz-wedge beam splitter was used to photograph filament formation of the Stokes (anti-Stokes) side of the spectra; three type 3-68 and three type 3-67 (two type 5-60) Corning filters were used to prevent the 530-nm direct laser light from entering the spectrograph. To reduce nonfilament light, a wire 2 mm in diameter was sometimes placed at the focal point of the imaging lens. Previously, spectra were taken on Polaroid type 57 film. At present, video systems such as an Silicon-intensified target (SIT) camera together with a PC computer are commonly used to display the spectra. Today, to obtain temporal information about the supercontinuum, a streak camera is added to the experimental system.

4. Generation of Supercontinuum in Solids

In the following sections, we review the experimental measurements of supercontinuum generated in condensed matter. Topics discussed include supercontinuum generation in various kinds of solids and liquids, optical glass fibers, liquid argon, liquid and solid krypton, magnetic crystals, and dielectric crystals.

The mechanisms behind SPM are discussed in Chapter 1 by Shen and Yang. In general, various mechanisms are responsible for SPM in condensed matter and give rise to the coefficient of the intensity-dependent refractive index n_2 . These are the orientational Kerr effect, electrostriction, molecular redistribution, librations, and electronic distribution. In suitably chosen media (central-symmetric molecules) these frequency-broadening mechanisms may be distinguished from the electronic mechanism through their dif-

ferent time responses (Lallemand, 1966). The relation times for these mechanisms are given approximately by (Brewer and Lee, 1968)

$$\tau(\text{orientation}) = \frac{4\pi}{3} \eta a^3 / kT > 10^{-12} \text{ s}, \quad (18)$$

$$\tau(\text{molecular types}) = \frac{\langle x^2 \rangle}{D} = \frac{6\pi\eta a \langle x^2 \rangle}{kT} > 10^{-12} \text{ s}, \quad (19)$$

$$\tau(\text{libration about field}) = \sqrt{\frac{2I}{\alpha E_0^2}} > 10^{-12} \text{ s}, \quad (20)$$

$$\tau(\text{electronic}) = \frac{2\pi a_0 \hbar}{e^2} > 1.5 \times 10^{-16} \text{ s}, \quad (21)$$

where η is the viscosity ($\eta = 0.4 \text{ cp}$ for liquids and $\eta = 10^6 \text{ cp}$ for glasses); a is the molecular radius; D is the diffusion coefficient ($\geq 10^{-5} \text{ cm}^2/\text{s}$ for liquids) and x is the diffusion distance of the clustering, $\sim 10^{-8} \text{ cm}$; I is the moment of inertia, $I_{\text{argon}} = 9.3 \times 10^{-38} \text{ esu}$ and $I_{\text{CCl}_4} = 1.75 \times 10^{-38} \text{ esu}$; α is the polarizability, $\alpha_{\text{argon}} = 1.6 \times 10^{-24} \text{ esu}$ and $\alpha_{\text{CCl}_4} = 1.026 \times 10^{-24} \text{ esu}$; and E_0 is the amplitude of the electric field, taken as 10^5 esu , which is close to the atomic field. The response time for an electron distortion is about the period of a Bohr orbit, $\sim 1.5 \times 10^{-16} \text{ s}$. Thus, typical calculated relaxation time responses for diffusional motions are $> 10^{-12} \text{ s}$, while the electronic distortion response time is $\sim 150 \text{ as}$.

With picosecond light pulses Brewer and Lee (1968) showed that the dominant mechanism for filament formation should be electronic in very viscous liquids. Molecular rocking has been suggested as the cause of broadening and self-focusing in CS_2 . The molecules are driven by the laser field to rock about the equilibrium position of a potential well that has been set up by the neighboring molecules. This mechanism is characterized by a relaxation time:

$$\tau_1 = \frac{\eta}{G} = 2.3 \times 10^{-13} \text{ s}, \quad (22)$$

where G is the shear modulus $\sim 1.5 \times 10^{10} \text{ dynes/cm}^2$ and viscosity $\eta = 3.7 \times 10^{-3} \text{ p}$ for CS_2 .

In solids, mechanisms giving rise to the coefficient of the intensity-dependent refractive index n_2 for picosecond pulse excitation are either direct distortion of electronic clouds around nuclei or one of several coupled electronic mechanisms: librational distortion, where electronic structure is distorted as the molecule rocks; electron-lattice distortion, where the electron cloud distorts as the lattice vibrates; and molecular distortion, where electronic shells are altered as the nuclei redistribute spatially. The electrostriction mechanism is rejected because it exhibits a negligible effect for picosecond and femtosecond pulses.

Typical supercontinuum spectra generated in solids and liquids using 8-ps pulses at 530 nm are displayed in Figure 2.4. All continuum spectra are similar despite the different materials.

4.1 Supercontinuum in Glasses

Spectra from the glass samples show modulation (see Figure 2.4a). The spectral modulation ranged from as small as a few wave numbers to hundreds of wave numbers. The filament size was approximately 5 to 50 μm . Typically, 5 to 20 small-scale filaments were observed. Occasionally, some laser output pulses from the samples did not show modulation or had no regular modulation pattern. Typical Stokes sweeps from these filaments were 1100 cm^{-1} in extradense flint glass of length 7.55 cm and 4200 cm^{-1} in both borosilicate crown (BK-7) and light barium (LBC-1) glass of length 8.9 cm. Sweeps on the anti-Stokes side were typically 7400 cm^{-1} in BK and LBC glasses. The sweep is polarized in the direction of the incident laser polarization for unstrained glasses.

4.2 Supercontinuum in Quartz

SPM spectra from quartz using an 8-ps pulse at 530 nm are similar to the spectra from glasses displayed in Figure 2.4a. Typical Stokes sweeps from the filaments were 3900 cm^{-1} in a quartz crystal of length 4.5 cm, and the anti-Stokes sweeps were 5500 cm^{-1} .

4.3 Supercontinuum in NaCl

Sweeps of 3900 cm^{-1} in NaCl of length 4.7 cm to the red side of 530 nm were observed. Sweeps on the anti-Stokes side were about 7300 cm^{-1} . Some of the spectra show modulation with ranges from a few wave numbers to hundreds of wave numbers. Some laser shots showed no modulation or no regular modulation pattern. For unstrained NaCl, the supercontinuum light is polarized in the direction of the incident laser polarization.

4.4 Supercontinuum in Calcite

Sweeps of 4400 cm^{-1} and 6100 cm^{-1} to the Stokes and anti-Stokes sides of 530 nm were observed in a calcite crystal of length 4.5 cm (see Figure 2.4b). Some spectra showed modulation structure within the broadened spectra; some showed no modulation or no regular modulation pattern. The exit supercontinuum light has same polarization as the incident laser. The SRS threshold is lower for laser light traveling as an O-wave than an E-wave. SPM dominates the E-wave spectra.

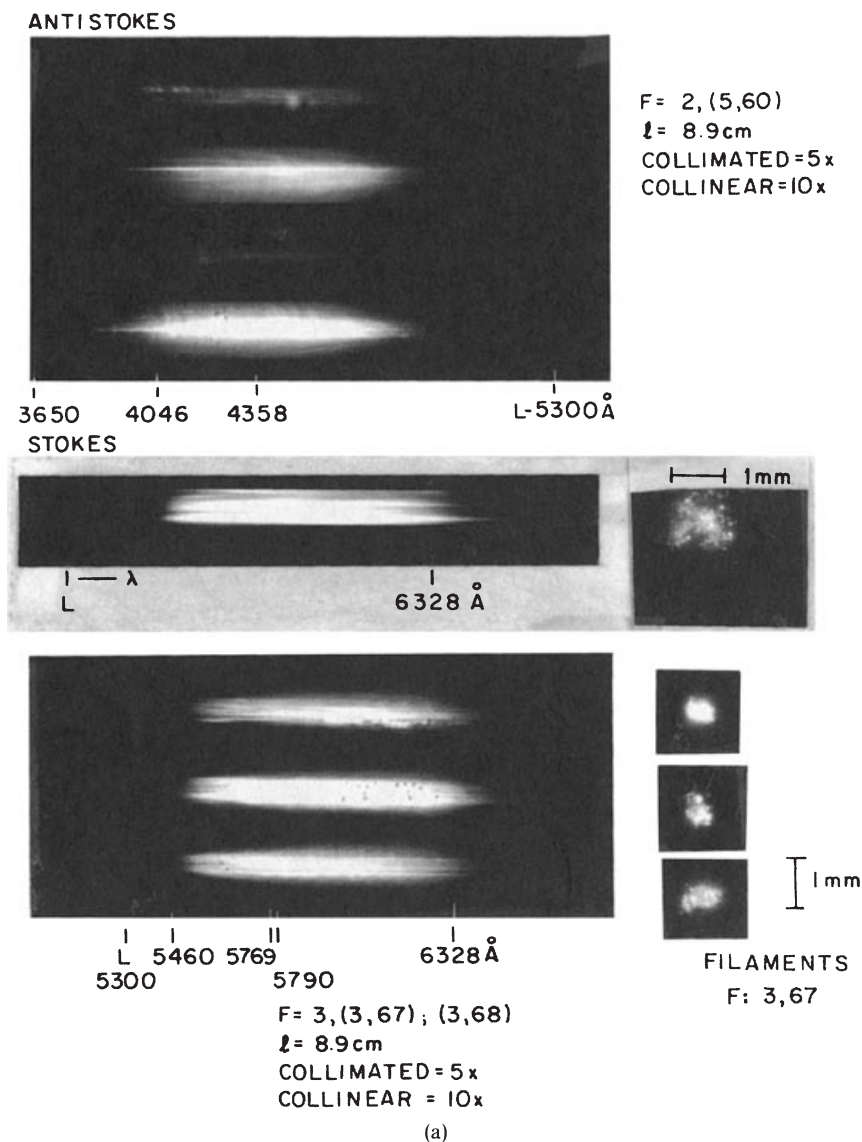


FIGURE 2.4. Supercontinuum spectra from various kind of solids and liquids. (a) Stokes and anti-Stokes SPM from BK-7 glass and filament formation for different laser shots. The filaments are viewed through Corning 3-67 filters. (b) Stokes and anti-Stokes SPM from calcite for different laser shots. The laser beam propagates as an O-wave through the sample. (c) Stokes and anti-Stokes SPM spectra from calcite for different laser shots. The laser beam propagates as an E-wave. (From Alfano, 1972.)

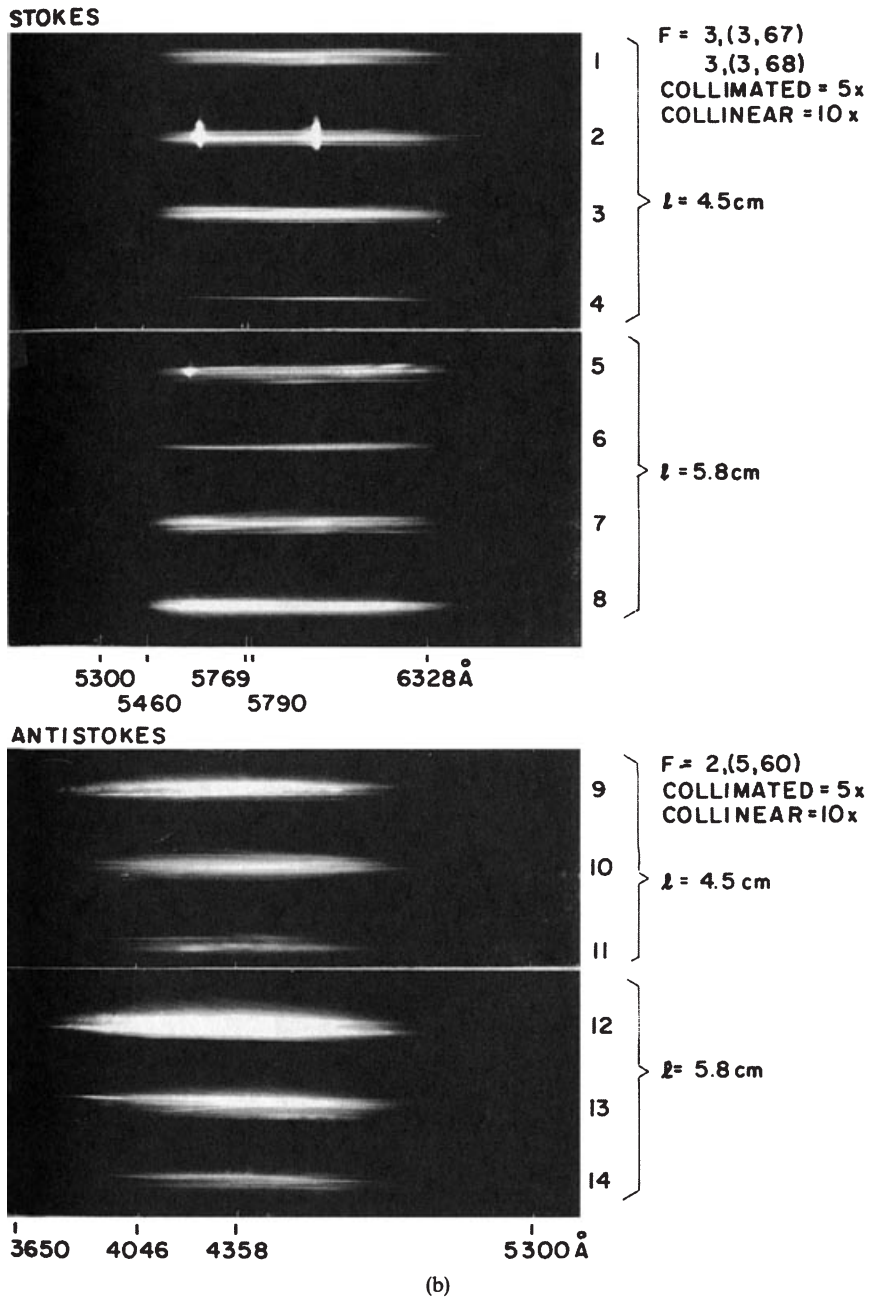
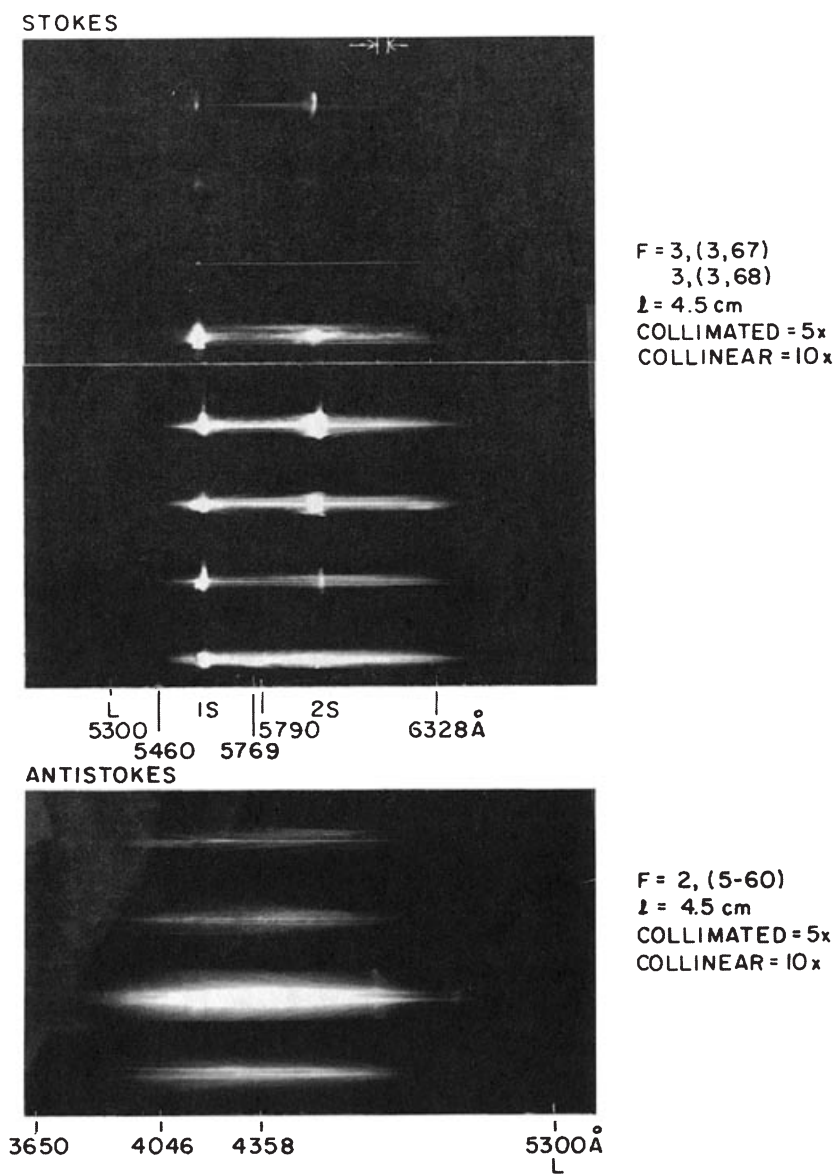


FIGURE 2.4. (continued)



(c)

FIGURE 2.4. (continued)

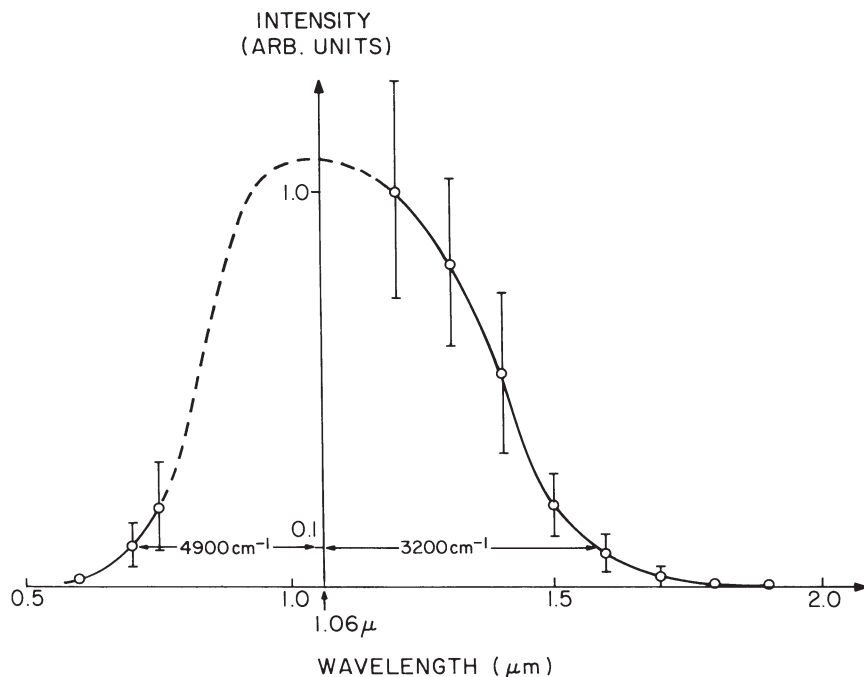


FIGURE 2.5. Relative emission intensity versus emission wavelength for KBr. Exciting wavelength = $1.06\mu\text{m}$. (From Yu et al., 1975.)

4.5 Supercontinuum in KBr

A high-power broadband coherent source in the near- and medium-infrared region can be realized by passing an intense $1.06\text{-}\mu\text{m}$ picosecond pulse through a KBr crystal. Figure 2.5 shows the spectra from 10-cm-long KBr crystal with excitation of a 9-ps, 10^{11} W/cm^2 pulse at $1.06\mu\text{m}$. On the Stokes side the maximum intensity occurs at $1.2\mu\text{m}$. When the signal drops to 10^{-1} the span of the spectral broadening is $\Delta\nu_s = 3200\text{ cm}^{-1}$ on the Stokes side and $\Delta\nu_a = 4900\text{ cm}^{-1}$ on the anti-Stokes side. Beyond $1.6\mu\text{m}$ the signal level falls off rapidly. At $1.8\mu\text{m}$ the signal is 10^{-2} and at $2\mu\text{m}$ no detectable signal can be observed (Yu et al., 1975).

4.6 Supercontinuum in Semiconductors

Infrared supercontinuum spanning the range 3 to $14\mu\text{m}$ can be obtained when an intense picosecond pulse generated from a CO_2 laser is passed into GaAs, AgBr, ZnSe, and CdS crystals (Corkum et al., 1985).

The supercontinuum spectra measured from a 6-cm-long Cr-doped GaAs crystal and a 3.8-cm AgBr crystal for different laser pulse durations and

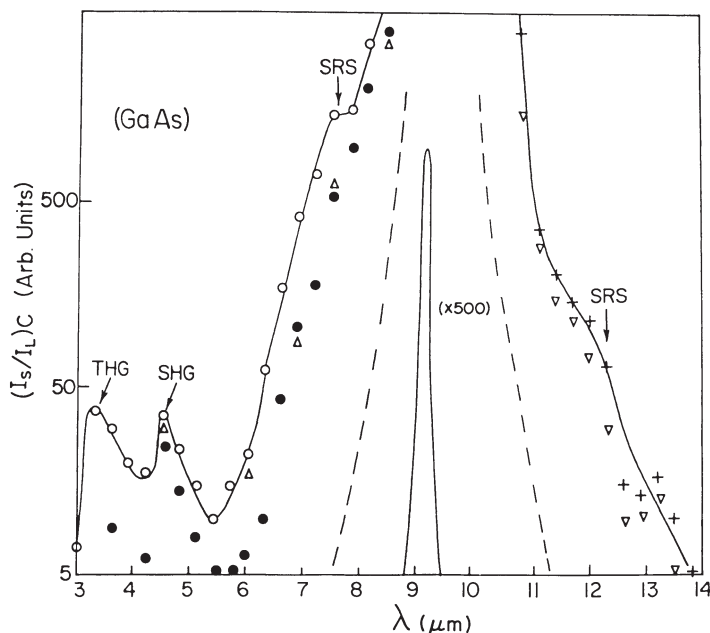


FIGURE 2.6. Supercontinuum spectra from a 6-cm-long Cr-doped GaAs crystal. (From Corkum et al., 1985.)

intensities and plotted in Figures 2.6 and 2.7, respectively. The signals were normalized for the input laser energy and the spectral sensitivity of filters, grating, and detectors. Each point represents the average of three shots. The salient feature of the curves displayed in Figures 2.6 and 2.7 is that the spectral broadening spans the wavelength region from 3 to $14\mu\text{m}$. The wave number spread on the anti-Stokes side is much greater than that on the Stokes side. From data displayed in Figure 2.6, the maximum anti-Stokes spectral broadening is $\Delta\omega_a = 793\text{cm}^{-1}$. Including second and third harmonic generation (SHG and THG), it spans 2000cm^{-1} . On the Stokes side, $\Delta\omega_s = 360\text{cm}^{-1}$, yielding a value of $\delta\omega_a/\delta\omega_s \sim 2.2$. For AgBr, Figure 2.7 shows that $\Delta\omega_a = 743\text{cm}^{-1}$ and $\Delta\omega_s = 242\text{cm}^{-1}$, yielding $\Delta\omega_a/\Delta\omega_s \sim 3$.

The spectral broadening mechanism for the supercontinuum can originate from several nonlinear optical processes. These include self-phase modulation, the four-wave parametric effect, higher-order harmonic generation, and stimulated Raman scattering. In Figure 2.6 the supercontinuum from the GaAs has two small peaks at 4.5 and $3.3\mu\text{m}$. These arise from the SHG and THG, respectively. Small plateaus are located at 7.5 and $12\mu\text{m}$. These arise from the first-order anti-Stokes and Stokes stimulated Raman scattering combined with SPM about these wavelengths. The SPM is attributed to an electronic mechanism.

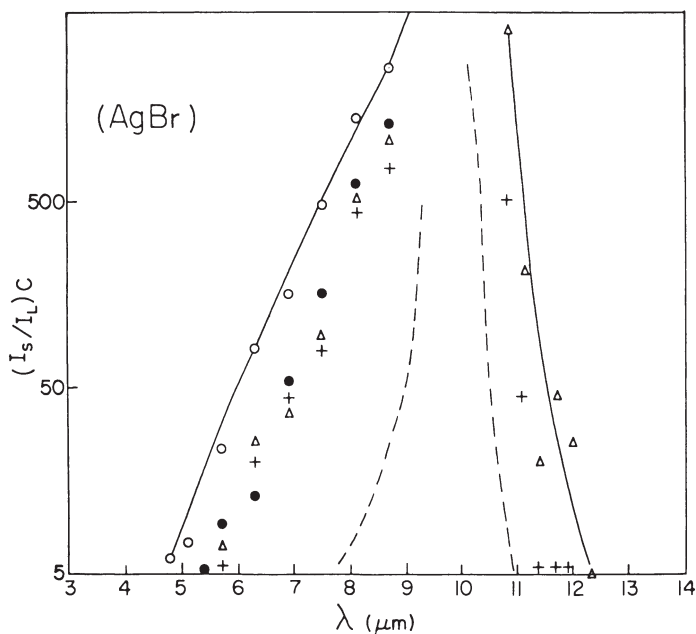


FIGURE 2.7. Supercontinuum spectra from a 3.8-cm-long AgBr crystal. (From Corkum et al., 1985.)

Summarizing the important experimental aspects of the spectra in condensed matter: The spectra are characterized by very large spectral widths and a nonperiodic or random substructure. Occasionally, a periodic structure interference minimum and maximum are observed. The modulation frequencies range from a few cm^{-1} to hundreds of cm^{-1} , and some modulation progressively increases away from the central frequency. The Stokes and anti-Stokes spectra are approximately equal in intensity and roughly uniform. The extents on the Stokes and anti-Stokes sides are not symmetric. The peak intensity at the central frequency is 10^2 – 10^3 the intensity of the SPM spectra at a given frequency.

5. Generation of Supercontinuum in Liquids

Nonlinear optical effects in solids are very effective; however, damage generated in solid media often limits their usefulness for ultrashort high-power effects. Various kinds of inorganic and organic liquids are useful media for generating picosecond or femtosecond supercontinuum light pulses since they are selfhealing media. The supercontinuum spectra produced in liquids (Alfano, 1972) are similar to the spectra displayed in Figure 2.4 (Alfano,

1972). The following highlights the supercontinuum phenomena in the various favorite liquid media of the authors. These liquids give the most intense and uniform supercontinuum spectral distributions.

5.1 Supercontinuum in H_2O and D_2O

The supercontinuum generated in H_2O and D_2O by the second harmonic of a mode-locked neodymium glass laser spanned several thousand wave numbers. The time duration was equal to or less than the picosecond pulse that generated it (Busch et al., 1973). The continuum extended to below 310 nm on the anti-Stokes side and to the near-IR region on the Stokes side. There were sharp absorptions at 450 nm in the H_2O continuum and at 470 nm in the D_2O continuum resulting from the inverse Raman effect (Alfano and Shapiro, 1970b; Jones and Stoicheff, 1964). Focusing a 12-mJ, 1060-nm single pulse 14 ps in duration into 25 cm of liquid D_2O resulted in a continuum that showed practically no structure, extending from 380 to at least 800 nm and highly directional and polarized (Sharma et al., 1976). Enhancing the supercontinuum intensity using water with ions is discussed in Section 10.

5.2 Supercontinuum in CCl_4

Another favorite liquid for producing a supercontinuum is CCl_4 , in which the spectra produced are similar to the spectra displayed in Figure 2.4. A typical flat white supercontinuum extending from 430 nm through the visible and near infrared could be produced by focusing an 8-ps pulse at 1060 nm with about 15 mJ pulse energy into a cell containing CCl_4 (Magde and Windsor, 1974).

5.3 Supercontinuum in Phosphoric Acid

Orthophosphoric acid was found to be a useful medium for generating picosecond continuum light pulses ranging from the near UV to the near IR. By focusing a pulse train from a mode-locked ruby laser into a 10-cm-long cell containing phosphoric acid (60% by weight) solution in water by an 8-cm focal lens, a supercontinuum from near 450 nm to the near IR was obtained. The supercontinuum spectra contain structure arising from Raman lines (Kobayashi, 1979).

5.4 Supercontinuum in Polyphosphoric Acid

The supercontinuum from polyphosphoric acid was generated by focusing an optical pulse at 694.3 nm with 100 mJ pulse energy and a pulse width of 28 ps into a cell of any length from 2 to 20 cm containing polyphosphoric acid. It reaches 350 nm on the anti-Stokes side, being limited by the absorp-

tion of polyphosphoric acid, and 925 nm on the Stokes side, being cut off by limitations of IR film sensitivity (Nakashima and Mataga, 1975).

6. Supercontinuum Generated in Optical Fibers

The peak power and the interaction length can be controlled better in optical fibers than in bulk materials. Optical fibers are particularly interesting material for nonlinear optical experiments. In this section, we discuss supercontinuum generation in glass optical fibers. Details of the use of SPM for pulse compression are discussed in other chapters.

The generation of continua in glass optical fibers was performed by Stolen et al. in 1974. Continua covering $\sim 500\text{ cm}^{-1}$ were obtained. Shank et al. (1982) compressed 90-fs optical pulses to 30-fs pulses using SPM in an optical fiber followed by a grating compressor. Using the SPM in an optical fiber with a combination of prisms and diffraction gratings, they were able to compress 30 fs to 6 fs (Fork et al., 1987; also see Chapter 10 by Johnson and Shank).

A typical sequence of spectral broadening versus input peak power using 500-fs pulses (Baldeck et al., 1987b) is shown in Figure 2.8. The spectra show

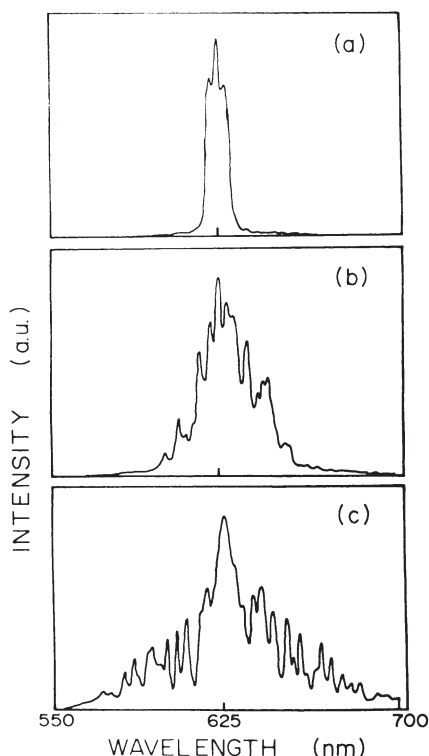


FIGURE 2.8. Sequence of spectral broadening versus increasing input energy in a single-mode optical fiber (length = 30 cm). The intensity of the 500-fs pulse was increased from (a) to (c). (From Baldeck et al., 1987b.)

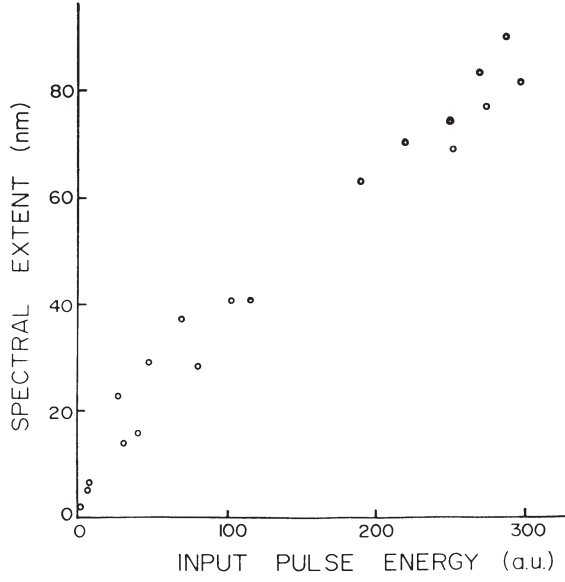


FIGURE 2.9. Supercontinuum spectra versus input pulse energy in a single-mode optical fiber (length = 30 cm) for a 500-fs pulse. (From Baldeck et al., 1987b.)

SPM characteristic of heavy modulation. The spectral extent is plotted against the energy in Figure 2.9 for 500-fs pulses (Baldeck et al., 1987b). The relative energy of each pulse was calculated by integrating its total broadened spectral distribution. The supercontinuum extent increased linearly with the pulse intensity. The fiber length dependence of the spectral broadening is plotted in Figure 2.10. The broadening was found to be independent of the length of the optical fiber for $l > 20$ cm. This is due to group velocity dispersion. The SPM spectral broadening occurs in the first few centimeters of the fiber for such short pulses (Baldeck et al., 1987b).

In multimode optical fibers, the mode dispersion is dominant and causes pulse distortion. Neglecting the detailed transverse distribution of each mode, the light field can be expressed by

$$E(t) = \sum_i a_i A_i(t) \exp[i\omega_0 t - ik_i z], \quad (23)$$

where ω_0 is the incident laser frequency; a_i , $A_i(t)$, and $k_i = n_i \omega_0 / c$ are the effective amplitude, electric field envelope function at the local time $\tau = t - z/v_{gi}$, and wave number of mode i , respectively; and v_{gi} is the group velocity of mode i . The effective refractive index of mode i is denoted by n_i and

$$n_i = n_{0i} + n_{2i} |E(t)|^2, \quad (24)$$

where n_{0i} and n_{2i} are the linear refractive index and the nonlinear coefficient of the i th mode, respectively. The nonlinearities of different modes are

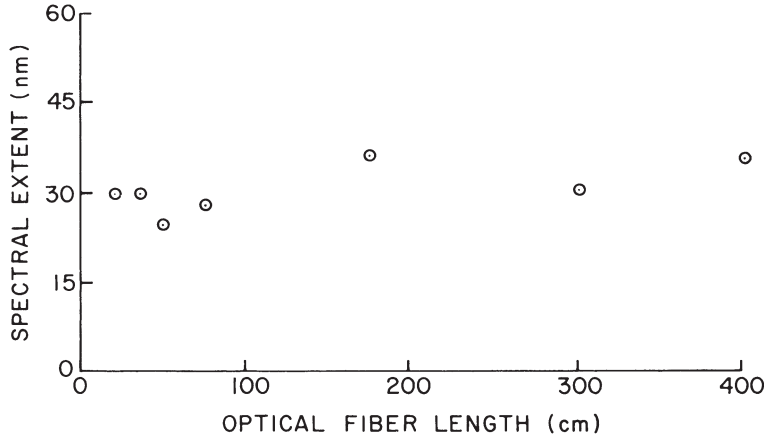


FIGURE 2.10. Supercontinuum spectra versus optical fiber length for a 500-fs pulse. (From Baldeck et al., 1987b.)

assumed to be the same, that is, $n_{2i} = n_2$. Substituting Eq. (21) into Eq. (20), we obtain

$$E(t) = \sum_i a_i A_i(t) \exp[i\omega_0 t - in_{0i}\omega_0 z/c - i\Delta\phi(t)], \quad (25)$$

where

$$\Delta\phi(t) = (n_2\omega_0 z/c)|E(t)|^2. \quad (26)$$

After inserting Eq. (23) into Eq. (26), the time-dependent phase factor $\Delta\phi(t)$ can be expanded in terms of $E_i(t)$:

$$\Delta\phi(t) = \sum_i \sum_j (n_2\omega_0 z/c) a_i a_j A_i(t) A_j(t) \exp[i(n_{0i} - n_{0j})\omega_0 z/c]. \quad (27)$$

In the picosecond time envelope, the terms of $i \neq j$ oscillate rapidly. Their contributions to the time-dependent phase factor are washed out. The approximate $\Delta\phi(t)$ has the form

$$\Delta\phi = \sum_i (n_2\omega_0 z/c) a_i^2 A_i^2(t). \quad (28)$$

The pulse shape changes due to the different group velocities of various modes. When most of the incident energy is coupled into the lower modes, the pulse will have a fast rising edge and a slow decay tail since the group velocity is faster for lower-order mode. This feature was observed using a streak camera. Therefore, the $\Delta\phi(t, z)$ of Eq. (28) will also have a fast rising edge and a slow decay tail. The time derivative of the phase $\Delta\phi(t, z)$ yields an asymmetric frequency broadening.

Figure 2.11 shows the spectral continuum generated from multimode glass optical fibers using 8-ps pulses at 530 nm. The spectral broadening is asym-

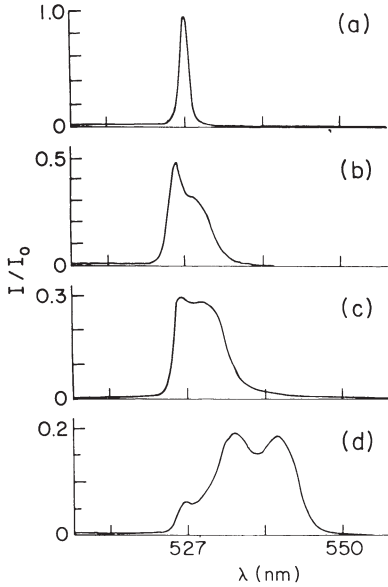


FIGURE 2.11. Output spectra for 8-ps laser pulses at 527 nm propagating through different lengths of multimode optical fibers: (a) no fiber; (b) 22 cm; (c) 42 cm; (d) 84 cm. (From Wang et al., 1988.)

metric about the incident laser frequency. It is shifted much more to the Stokes side than to the anti-Stokes side. The observed spectra did not show a modulation. This can be explained by the spectral resolution of the measurement system. The calculated modulation period is about 0.13 nm, which is much smaller than the resolution of the measurement system (about 1 nm) (Wang et al., 1988).

7. Supercontinuum Generation in Rare-Gas Liquids and Solids

Continuum generation is a general phenomenon that occurs in all states of matter. A system for testing the role of the electronic mechanism is rare-gas liquids and solids (Alfano and Shapiro, 1970a). Rare-gas liquids are composed of atoms possessing spherical symmetry. Thus, there are no orientational, librational, or electron-lattice contributions to the nonlinear refractive index n_2 . However, interrupted rocking of argon can occur in which a distorted atom can rock about an equilibrium value before it collides with other atoms. Contributions to the nonlinear refractive index might be expected from electrostriction, molecular redistribution, interrupted rocking, and a distortion of the electron clouds:

$$n_2 = n_{2\text{ELECTRONIC}} + n_{2\text{MR}} + n_{2\text{LIBRATION}} + n_{2\text{ELECTROSTR}}. \quad (29)$$

Electrostriction is ruled out because picosecond exciting pulses are too short. Molecular redistribution arises from fluctuations in the local positional

arrangement of molecules and can contribute significantly to n_2 . However, n_2 due to all mechanisms except electronic was estimated to be $\sim 2 \times 10^{-14}$ esu for liquid argon from depolarized inelastic-scattering data. Electronic distortion ($n_2 = 6 \times 10^{-14}$ esu) slightly dominates all nonlinear index contributions (Alfano and Shapiro, 1970a; Alfano, 1972). Furthermore, the depolarized inelastic light-scattering wing vanishes in solid xenon, implying that the molecular redistribution contribution to n_2 vanishes in rare-gas solids. Observations of self-focusing and SPM in rare-gas solids appear to provide a direct

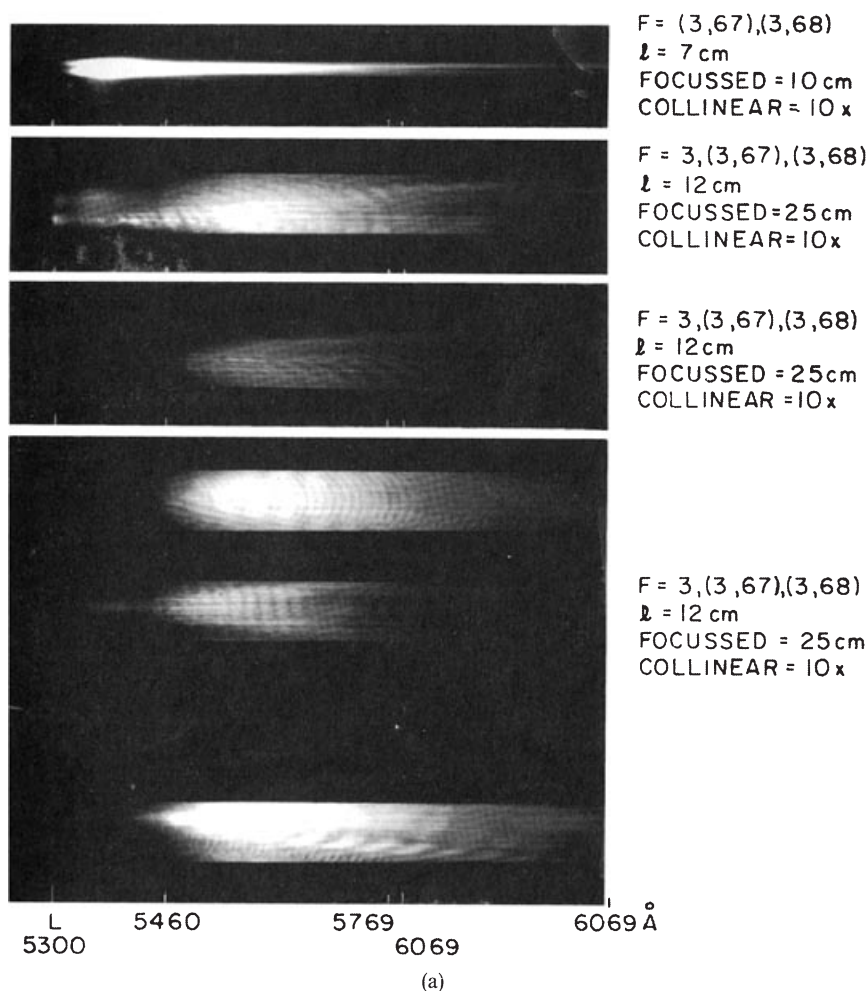


FIGURE 2.12. Supercontinuum spectra for picosecond laser pulses at 530 nm passing through rare-gas liquids and solids; (a) Stokes SPM from liquid argon for different laser shots; (b) anti-Stokes SPM for liquid argon for different laser shots; (c) Stokes SPM for liquid and solid krypton for different laser shots. (From Alfano, 1972.)

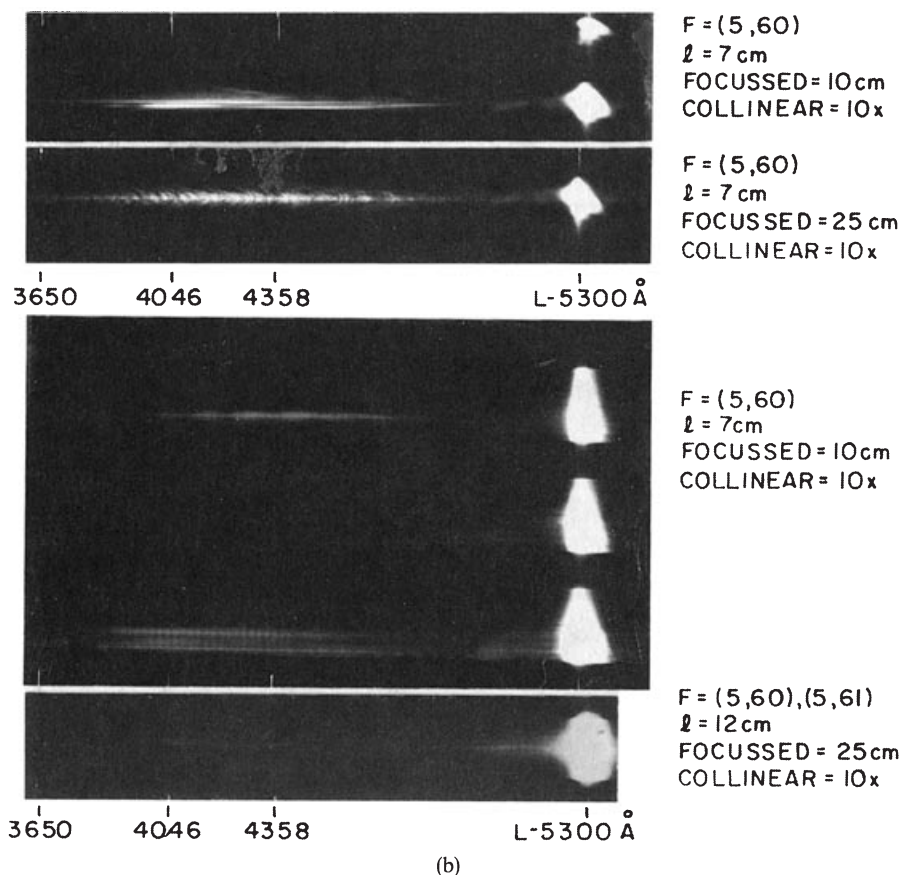


FIGURE 2.12. (continued)

proof that atomic electronic shells are distorted from their spherical symmetry under the action of the applied field. However, both pure electronic and molecular redistribution mechanisms contribute to n_2 in rare-gas liquids. The response time of the system for a combination of both of these mechanisms lies between 10^{-15} and 10^{-12} s. For femtosecond and subpicosecond pulses, the dominant mechanism for n_2 and SPM is electronic in origin.

The experimental setup used to generate and detect a supercontinuum in rare-gas liquids and solids is the same as that shown in Figure 2.3 with the exception that the samples are placed in an optical dewar.

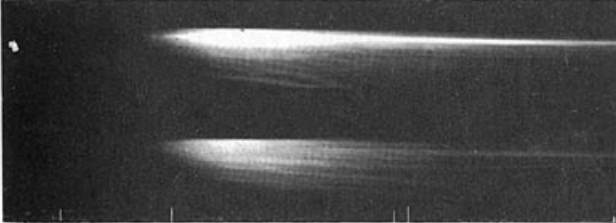
Typical supercontinuum spectra from rare-gas liquids and solids are displayed in Figure 2.12. Sweeps of 1000 to 6000 cm^{-1} were observed to both the Stokes and anti-Stokes sides of 530 nm in liquid argon. Modulation ranges from a few cm^{-1} to hundreds of cm^{-1} . Similar spectral sweeps were observed in liquid and solid krypton.

KRYPTON: STOKES

LIQUID



SOLID



5300 5460 5769 5769 6069

$F=3, (367)(368)$
 $l=12\text{ cm}$
 $\text{FOCUSSED}=25\text{ cm}$
 $\text{COLLINEAR}\approx 5\times$

(c)

FIGURE 2.12. (continued)

A most important point is that the threshold for observing SPM in liquid krypton is 0.64 ± 0.12 that in liquid argon. The SPM threshold ratio of solid and liquid krypton is 0.86 ± 0.15 . In liquid argon, SPM spectra appear at a threshold power of $\sim 0.5\text{ GW}$ focused in a 12-cm sample. The swept light is also collimated, polarized, and modulated. These observations rule out dielectric breakdown.

The refractive index in rare-gas liquids is given by $n_{\parallel} = n_0 + n_2 \langle E^2 \rangle$, where n_{\parallel} is the refractive index parallel to the field. $\langle E^2 \rangle^{1/2}$ is the rms value of the electric field. The electronic nonlinear refractive index in rare gas liquids is given by

$$n_2 = [(n_0^2 + 2)^4 / 81n_0] \pi N \rho, \quad (30)$$

where n_0 is the linear refractive index, ρ is the second-order hyperpolarizability, and N is the number of atoms per unit volume. The term $n_2 = 0.6 \times 10^{-13}$ esu in liquid argon and $\approx 1.36 \times 10^{-13}$ in liquid krypton. For liquid argon

and liquid and solid krypton, the refractive indices are taken as 1.23, 1.30, and 1.35, respectively (McTague et al., 1969). Intense electric fields distort atoms and produce a birefringence. The anisotropy in refractive index between light traveling with the wave vector parallel and perpendicular to the applied electric field is given by (Alfano, 1972)

$$\delta n_{\parallel} - \delta n_{\perp} = \frac{1}{3} n_2 E_0^2, \quad (31)$$

where δn_{\parallel} and δn_{\perp} are the changes in refractive indices parallel and perpendicular to the field. The value of $n_2 E_0^2$ is $\sim 5 \times 10^{-5}$ V/m in liquid argon when $E_0 \sim 1.5 \times 10^7$ V/m ($\sim 4 \times 10^{11}$ W/cm²). This change in index explains the self-focusing and SPM described above which was observed by Alfano and Shapiro in 1970. Similar SPM effects occur in organic and inorganic liquids, often accompanied by SRS and inverse Raman effects.

8. Supercontinuum Generation in Antiferromagnetic KNiF₃ Crystals

The influence of magnetic processes on nonlinear optical effects is an interesting topic. In this section, we discuss the supercontinuum generation associated with the onset of magnetic order in a KNiF₃ crystal (Alfano et al., 1976). Light at 530 nm is well suited for the excitation pulse because KNiF₃ exhibits a broad minimum in its absorption (Knox et al., 1963) between 480 and 610 nm.

Typical spectra from an unoriented 5-cm-long KNiF₃ single crystal are displayed in Figure 2.13 for 530-nm picosecond excitation (Alfano et al., 1976). The spectra are characterized by extensive spectral broadening ranging up to ~ 3000 cm⁻¹ to either side of the laser frequency. The intensity, although not the spectral broadening, of the output exhibited the large temperature dependence illustrated in Figure 2.14. There is no sharp feature at 552 nm, the position expected for stimulated Raman scattering by the 746-cm⁻¹ magnon pair excitation. Usually, the spectra were smooth; however, occasionally structure was observed. A periodic structure with a modulation frequency of tens to hundreds of wave numbers was evident. The frequency broadening light is also polarized in the same direction as the incident 530-nm pulse. This property is the same observed in glass, crystals, and liquids (see Sections 3–6). Self-focusing was also observed, usually in the form of 10 to 40 small self-focused spots 5 to 20 μ m in diameter at the exit face of the crystal. Using a focused beam, optical damage could also be produced. It should be emphasized that spectral broadening was always observed even in the absence of self-focusing, damage, or periodic spectral intensity modulation.

Figure 2.15 shows the output intensity at 570 nm as a function of input intensity for two temperatures: above and below the Néel temperature. The output intensity is approximately exponential in the input intensity at both

FIGURE 2.13. Spectra for picosecond laser pulse at 530 nm passing through 5-cm-long KNiF_3 . (From Alfano et al., 1976.)

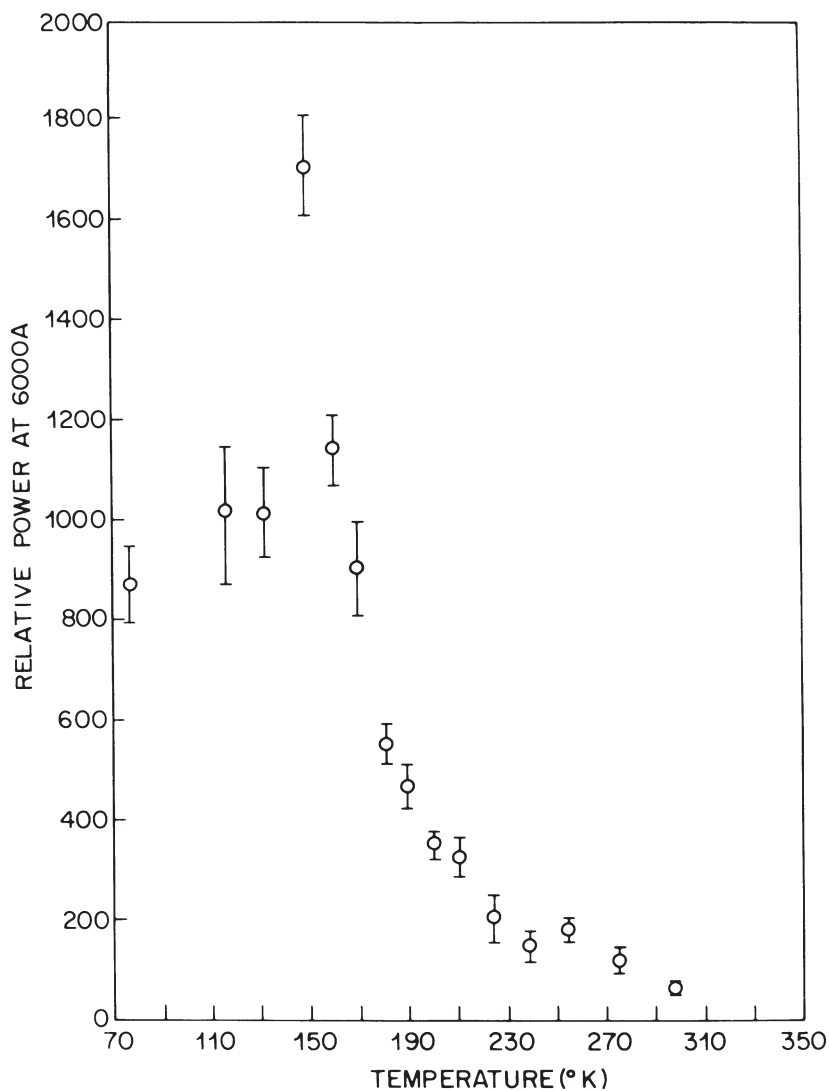
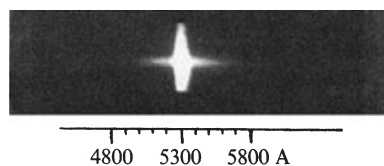


FIGURE 2.14. Intensity of the frequency-broadening emission from KNiF_3 as a function of temperature at fixed pump intensity at 552 nm. (From Alfano et al., 1976.)

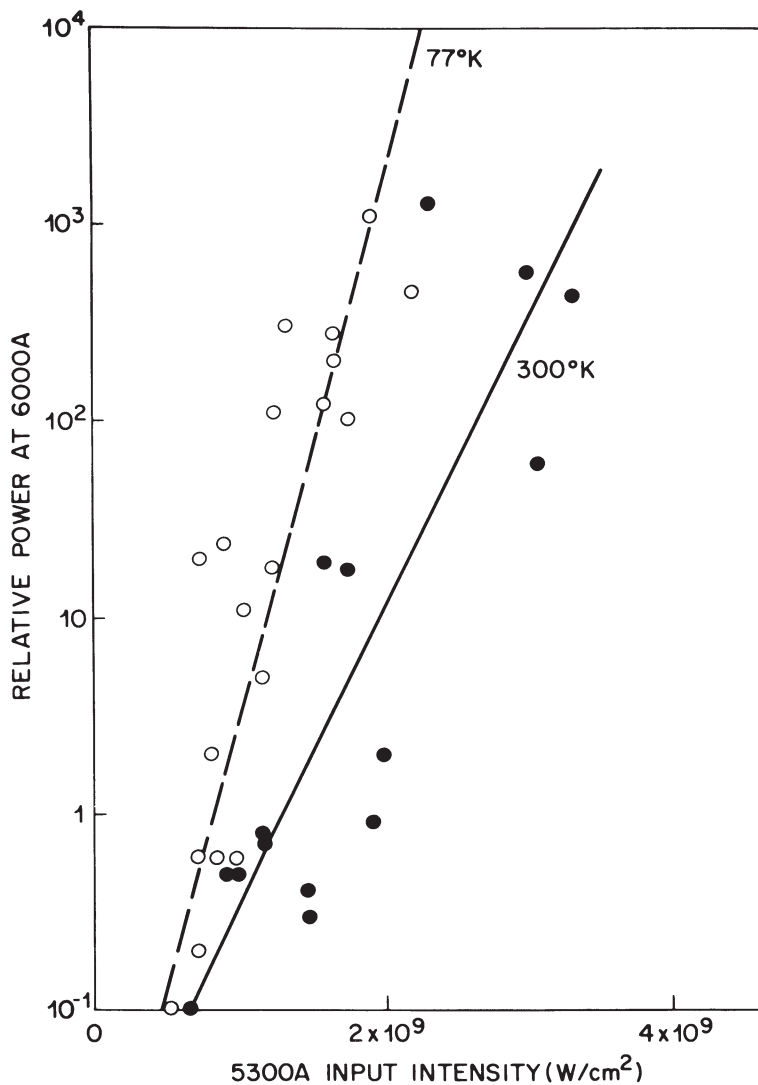


FIGURE 2.15. Intensity dependence of continuum spectra at 570 nm from KNiF_3 as a function of pumping laser intensity at fixed lattice temperature. (From Alfano et al., 1976.)

temperatures. However, the slope is more than a factor of two larger at 77 K than at 300 K. The rapid rise in conversion efficiency of four orders of magnitude within a small interval of input intensity is indicative of an amplification process with very large gain. Identical curves were obtained at 552 and 600 nm output wavelengths. The similarity in results for several output frequencies shows that simple stimulated magnon pair scattering is not the

dominant process. If it were, one would expect the behavior at 552 nm to differ considerably from that at other wavelengths.

The most novel experimental results in KNiF_3 are the large ($\sim 20\times$) intensity increases below T_N . Spectra at 552, 570, and 600 nm behave identically—within experimental error—consistent with the observations in Figure 2.15. The temperature dependence of the relative **peak** intensity for the spontaneous magnon pair scattering in the KNiF_3 sample (using 514.5 nm laser light) was measured and is potted in Figure 2.14. For KNiF_3 the magnon pair scattering accounts for the entire inelastic light scattering and therefore for the non- σ electronic contribution to $\chi^{(3)}$ (Hellwarth et al., 1975). The temperature dependence is compelling evidence for the magnetic origin of the low-temperature-enhanced nonlinear optical spectral broadened intensity.

The observation can be semiquantitatively accounted for in terms of a temperature-dependent spin contribution to the overall nonlinear susceptibility $\chi_{ijkl}^{(3)}$ that governs four-photon parametric mixing as the primary process. In general $\chi^{(3)}$ may be written as a sum of electronic and Raman contributions (Levenson and Bloembergen, 1974). For KNiF_3 we may consider the latter to consist solely of the magnon pair Raman scattering contribution (Chinn et al., 1971; Fleury et al., 1975), which we can approximate as a Lorentzian:

$$\chi_{ijkl}^{(3)}(-\omega_3, \omega_1, \omega_1, -\omega_2) = \chi_E^{(3)} + K \frac{\alpha_{ij}^m \alpha_{kl}^m + \alpha_{il}^m \alpha_{jk}^m}{\omega_m - (\omega_1 - \omega_2) + i\Gamma_m}. \quad (32)$$

Here ω_m and Γ_m denote the temperature-dependent frequency and linewidth, respectively, of the magnon pair excitations, α_{ij}^m is the magnon pair polarizability, and $\chi_E^{(3)}$ is the usual nonresonant, temperature-independent “electronic” contribution from nonlinear distortion of the electronic orbits. The second term in Eq. (32) is called magnetic $\chi_M^{(3)}$. Since the **integrated intensity** of the spontaneous magnon pair Raman spectrum, which is $\sim |\alpha^m|^2$, has been measured and found to be essentially temperature independent (Chinn et al., 1971; Fleury et al., 1975), the only quantities in Eq. (32) that vary significantly with temperature are ω_m and Γ_m . The observed temperature independence of the extent of spectral broadening, $\delta\omega$, may be explained by noting that $\delta\omega \sim 2\Delta\omega n_2 k E_1^2 l$ due to self-phase modulation. Here $\Delta\omega$ is the spectral width of the input pulse, k is its propagation constant, E_1 is the field amplitude, and l is the path length. n_2 is the nonlinear refractive index, which contains a purely electronic contribution, σ , and a contribution proportional to the integrated Raman scattering cross section (Hellwarth et al., 1975). Since neither σ nor $|\alpha^m|^2$ is temperature dependent in KNiF_3 , n_2 and therefore $\Delta\omega$ should not vary either, in agreement with observations.

The observed strong temperature dependence of the intensity of the frequency-broadened spectrum (see Figure 2.14) arises from the resonant term in Eq. (32) through the primary process $2\omega_1 \rightarrow \omega_2 + \omega_3$, which is strongest when $\omega_2 = \omega_1 + \omega_m$ and increases as Γ_m decreases (on cooling below the Néel

temperature). That is, the resonant contribution to $\chi^{(3)}$ in Eq. (32) varies with temperature in the same way as the peak spontaneous magnon pair cross section: $\Gamma_m^{-1}(T)$. However, the individual contribution to $\chi^{(3)}$ cannot be directly inferred from the dependence of the broadened spectrum. This is because the latter receives significant contributions from secondary processes of the form $\omega_1 + \omega_2' \rightarrow \omega_3' + \omega_4$ etc., in which products of the primary process interact with the pump to smooth the spectral distribution and wash out the sharp features that the resonant spin nonlinearity produces in the primary process. The large values of pump intensity and source spectral width make possible strong amplification in spite of imprecise phase matching in the forward direction. Such behavior (washing out of stimulated Raman features by the spectral broadening process) has frequently been observed in both liquids and crystals. Thus a full quantitative description of the nonlinear optical processes in KNiF_3 is not yet possible.

9. Generation of Supercontinuum near Electronic Resonances in Crystals

Since the active medium of a laser possesses well-defined electronic energy levels, knowledge of SPM near electronic levels is of paramount importance. SPM near electronic levels of a PrF_3 crystal has been investigated experimentally and theoretically to gain additional information on the SPM process—in particular, on the role played by the electronic levels and on how the continuum spectrum evolves through and beyond the electronic absorption levels (Alfano et al., 1974).

Experimentally, the Stokes and anti-Stokes spectrum and filament formation from the PrF_3 crystal are investigated under intense picosecond pulse excitation at the wavelength of 530 nm. The c axis of the crystal is oriented along the optical axis. The intensity distribution at the exit face of the crystal is magnified by 10 \times and imaged on the slit of a Jarrell-Ash $\frac{1}{2}$ -m-grating spectrograph so that the spectrum of each filament can be displayed. The spectra are recorded on Polaroid type 57 film. No visible damage occurred in the PrF_3 crystal.

The PrF_3 crystal was chosen for the experiment because its electronic levels are suitably located on the Stokes and anti-Stokes sides of the 530-nm excitation wavelength. The absorption spectra of a $\frac{1}{2}$ -mm-thick PrF_3 crystal and the energy level scheme of Pr^{3+} ions are shown in Figure 2.16. The fluorides of Pr have the structure of the naturally occurring mineral tysonite with D_{3d}^4 symmetry.

Typical spectra of frequency broadening from PrF_3 about 530 nm are shown in Figure 2.17 for different laser shots. Because of the absorption associated with the electronic level, it is necessary to display the spectrum over different wavelength ranges at different intensity levels. In this manner, the

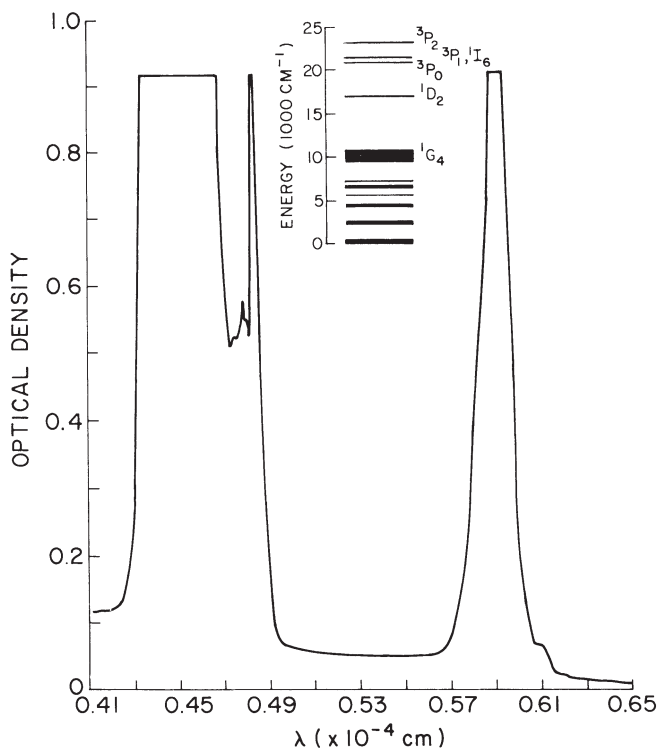


FIGURE 2.16. Absorption spectra of 0.5-mm-thick PrF_3 crystal; insert is the level scheme of Pr^{3+} ions. (From Alfano et al., 1974.)

development of the SPM spectrum through the electronic absorption levels can be investigated. Using appropriate filters, different spectral ranges are studied and displayed in the following figures: in Figure 2.18a the Stokes side for frequency broadening $\bar{\nu}_B > 100 \text{ cm}^{-1}$ at an intensity level (I_{SPM}) of $\sim 10^{-2}$ of the laser intensity (I_L), in Figure 2.18b the Stokes side for $\bar{\nu}_B > 1500 \text{ cm}^{-1}$ at $I_{\text{SPM}} \sim 10^{-4} I_L$, in Figure 2.18c the anti-Stokes side for $\bar{\nu}_B > 100 \text{ cm}^{-1}$ at $I_{\text{SPM}} \sim 10^{-2} I_L$, and in Figure 2.18d the anti-Stokes side for $\bar{\nu}_B > 1500 \text{ cm}^{-1}$ at $I_{\text{SPM}} \sim 10^{-4} I_L$. Usually 50 to 100 small-scale filaments 5 to 50 μm in diameter are observed.

Several salient features are evident in the spectra displayed in Figures 2.17 and 2.18. In Figure 2.17 the Stokes and anti-Stokes spectra are approximately equal in intensity and frequency extent. The peak intensity at the central frequency is ~ 100 times the intensity of the SPM at a given frequency. The extent of the frequency broadening is $\sim 1500 \text{ cm}^{-1}$, ending approximately at the absorption lines. Occasionally a periodic structure of minima and maxima is observed that ranges from a few cm^{-1} to 100 cm^{-1} , and for some observations no modulation is observed. Occasionally an absorption band appears on the

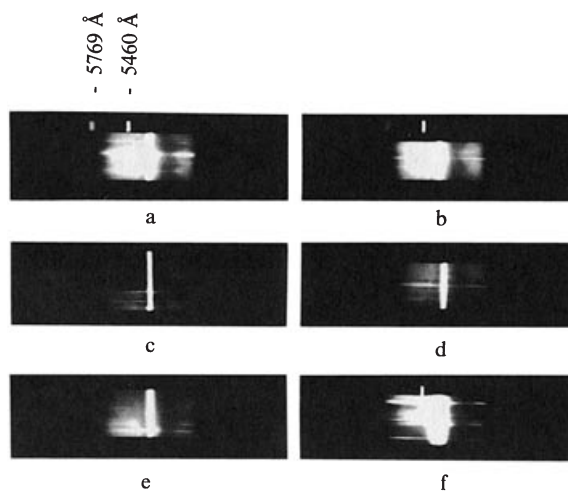


FIGURE 2.17. Spectra from PrF_3 excited by 4-ps laser pulses at 530 nm; neutral density (ND) filters: (a) ND = 1.5; (b) ND = 1.5; (c) ND = 2.0; (d) ND = 2.0; (e) ND = 1.7; (f) ND = 1.4. A wire is positioned after the collection lens at the focal length. (From Alfano et al., 1974.)

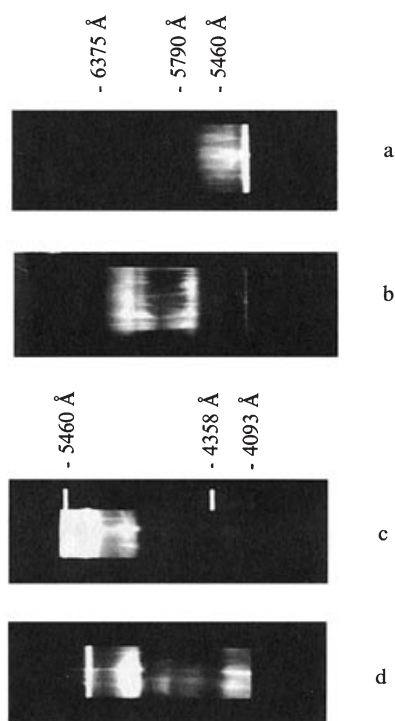
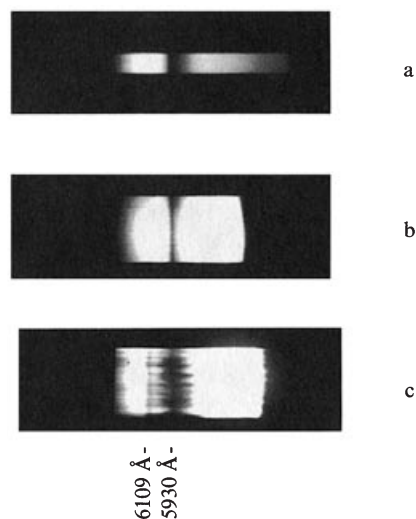


FIGURE 2.18. Spectra on the Stokes and anti-Stokes sides of the 530-nm excitation: (a) Stokes side, Corning 3-68 filter, wire inserted, ND = 2.0; (b) Stokes side, Corning 3-66 filter, wire inserted; (c) anti-Stokes side, wire inserted, ND = 1.0; (d) anti-Stokes side, Corning 5-61, wire inserted. (From Alfano et al., 1974.)

FIGURE 2.19. Comparison of the Stokes absorption spectra of PrF_3 photographed with different light sources: (a) light emitted from a tungsten lamp is passed through 0.5-cm-thick crystal; (b) SPM light emitted from BK-7 glass is passed through 0.5-mm-thick crystal; (c) SPM light is generated within the 5-cm PrF_3 . (From Alfano et al., 1974.)



anti-Stokes side of the 530-nm line whose displacement is 430 cm^{-1} . In Figure 2.18 the main feature is the presence of a much weaker super-broadband continuum whose frequency extends through and past the well-defined absorption lines of the Pr^{3+} ion to a maximum frequency of $>3000\text{ cm}^{-1}$ on the Stokes side (end of film sensitivity) and $>6000\text{ cm}^{-1}$ on the anti-Stokes side. The intensity of the continuum at a given frequency outside absorption lines is $\sim 10^{-4}$ the laser intensity.

The observed absorption lines on the anti-Stokes side of 530 nm are located at 441.5, 465.3, and 484.5 nm and on the Stokes side at 593 and 610.9 nm. These lines correspond within $\pm 0.7\text{ nm}$ to the absorption lines measured with a Cary 14. The absorption lines measured from the Cary spectra are $\sim 3\text{ cm}^{-1}$ at 611.2 nm, 62 cm^{-1} at 5938.8 nm, 46 cm^{-1} at 485.2 nm, and $>100\text{ cm}^{-1}$ at 441.2 nm. Figure 2.19 compares the Stokes absorption spectra of a PrF_3 crystal photographed with a $\frac{1}{2}$ -m Jarrell-Ash spectrograph with different broadband light sources. Figure 2.19a was obtained with light emitted from a tungsten lamp passing through a $\frac{1}{2}$ -mm PrF_3 crystal, Figure 2.19b was obtained with the Stokes side of the broadband picosecond continuum generated in BK-7 glass passing through a $\frac{1}{2}$ -mm PrF_3 , and Figure 2.19c was obtained with the broadband light generated in a 5-cm PrF_3 crystal. Notice that the absorption line at 611.2 nm is very pronounced in the spectra obtained with the continuum generated in PrF_3 , whereas with conventional absorption techniques it is barely visible. The anti-Stokes spectrum obtained with light emitted from a tungsten filament lamp passing through a $\frac{1}{2}$ -mm PrF_3 crystal is shown in Figure 2.20a. This is compared with the spectrum obtained with broadband light generated in a 5-cm PrF_3 crystal shown in Figure 2.20b.

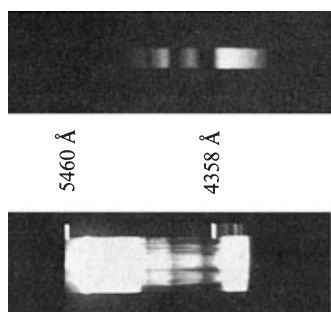


FIGURE 2.20. Comparison of the anti-Stokes absorption spectrum of PrF_3 photographed with (a) light emitted from a tungsten lamp passing through 0.5-mm-thick crystal and (b) SPM light generated within the 5-cm PrF_3 . (From Alfano et al., 1974.)

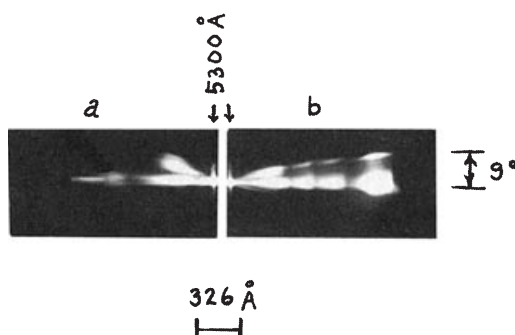


FIGURE 2.21. Angular variation of the (a) Stokes and (b) anti-Stokes spectral patterns emitted from PrF_3 crystal: (a) Corning 4(3-67) filters, ND = 1.0; (b) Corning 2(5-60) filters. (From Alfano et al., 1974.)

The angular variation of the anti-Stokes and Stokes spectral emission from PrF_3 is displayed in Figure 2.21. The light emitted from the sample is focused on the slit of a $\frac{1}{2}$ -m Jarrell-Ash spectrograph with a 5-cm focal length lens with the laser beam positioned near the bottom of the slit so that only the upper half of the angular spectrum curve is displayed. In this fashion, a larger angular variation of the spectrum is displayed. Emission angles $>9^\circ$ go off slit and are not displayed. This spectrum is similar to four-photon emission patterns observed from glass and liquids under picosecond excitation.

The experimental results show that a discontinuity in intensity occurs when the self-phase modulation frequency extends beyond the absorption line frequency. This is due to almost total suppression of the signal beyond the absorption resonance (Alfano et al., 1974). A similar argument and conclusion hold for the blue side of the laser line. The residual weak intensity that exists beyond the absorption line is not due to SPM. It can arise, however, from three-wave mixing. Since there was a continuum of frequencies created by SPM, it might be possible for three such frequencies, ω_1 , ω_2 , and ω_3 , to mix to create a signal at frequency $\omega_1 + \omega_2 - \omega_3$ that lies beyond the absorption line. Since the frequencies are chosen from a continuum, it is also possible for phase matching to be achieved. For the spectrum in the domain between the laser frequency and the absorption line, the extent of self-broadening is proportional to the intensity. Since the energy in the pulse is proportional to the product of the frequency extent and the intensity spectrum, the intensity spectrum remains approximately constant. The observed

absorption band in the continuum on the anti-Stokes side about 400 cm^{-1} away from the excitation frequency (see Figure 2.17) is probably due to the inverse Raman effect (Jones and Stoicheff, 1964). The observed absorption band is located in the vicinity of strong Raman bands: 401, 370, and 321 cm^{-1} .

A curious feature of the associated weak broadband spectrum is the existence of a pronounced absorption line at a position (611.2 nm) where the linear absorption would be expected to be rather weak. A possible explanation for this is as follows: Imagine tracing the spatial development of the phase modulation spectrum. At a short distance, where the bounds of the spectrum have not yet intersected a strong absorption line, the spectrum is reasonably flat. On intersecting the absorption line, the spectrum abruptly drops (Alfano et al., 1974). The mechanism of FFG is presumably responsible for the appearance of the signal beyond the absorption line limit. This explanation is also supported by the appearance of the angular emission pattern (see Figure 2.21). As the spectrum continues to develop, one reaches a point where the limit of the regenerated spectrum crosses a weak absorption line. One can again expect a drastic drop in the spectrum at the position of this line. At still greater distances renewed four-photon parametric regeneration accounts for the feeble signal. A continuum is generated behind absorption bands due to contributions from SPM, three-wave mixing (TWM), and FFG.

10. Enhancement of Supercontinuum in Water by Addition of Ions

The most common liquids used to generate a continuum for various applications are CCl_4 , H_2O , and D_2O . In most applications of the ultrafast supercontinuum, it is necessary to increase the conversion efficiency of laser excitation energy to the supercontinuum. One method for accomplishing this is based on the induced- or cross-phase modulation. Another way is to increase n_2 in materials. In this section, chemical means are used to obtain a tenfold enhancement of the ultrafast supercontinuum in water by adding Zn^{2+} or K^+ ions (Jimbo et al., 1987) for 8-ps pulse generation.

The optical Kerr gate (OKG) (Ho and Alfano, 1979) was used to measure the nonlinear refractive index of the salt solutions. The primary and second harmonic light beams were separated by a dichroic mirror and then focused into a 1-cm-long sample cell filled with the same salt solutions that produced the ultrafast supercontinuum pulse enhancements. The size of the nonlinear index of refraction, n_2 , was determined from the transmission of the probe beam through the OKG.

Three different two-component salt solutions of various concentrations were tasted. The solutes were KCl , ZnCl_2 , and K_2ZnCl_4 . All measurements were performed at $20 \pm 1^\circ\text{C}$. Typical spectra of ultrafast supercontinuum

pulses exhibited both SPM and FPPG features. The collinear profile arising from SPM has nearly the same spatial distribution as the incident 8-ps, 530-nm laser pulse. The two wings correspond to FPPG pulse propagation. The angle arises from the phase-matching condition of the generated wavelength emitted at different angles from the incident laser beam direction. FPPG spectra sometimes appear as multiple cones and sometimes show modulated features. SPM spectra also show modulated patterns. These features can be explained by multiple filaments.

Typical ultrafast supercontinuum pulse spectra on the Stokes side for different aqueous solutions and neat water, measured with the optical multi-channel analyzer, are shown in Figure 2.22. The salient features in Figure 2.22 are a wideband SPM spectrum together with the stimulated Raman scattering of the OH stretching vibration around 645 nm. The addition of salts causes the SRS signal to shift toward the longer-wavelength region and sometimes causes the SRS to be weak (Figure 2.22a). The SRS signal of pure water and dilute solution appears in the hydrogen-bonded OH stretching region ($\sim 3400\text{ cm}^{-1}$). In a high-concentration solution, it appears in the non-hydrogen-bonded OH stretching region ($\sim 3600\text{ cm}^{-1}$). The latter features of SRS were observed in an aqueous solution of NaClO_4 by Walrafen (1972).

To evaluate quantitatively the effect of cations on ultrafast supercontinuum generation, the ultrafast supercontinuum signal intensity for various samples at a fixed wavelength were measured and compared. Figure 2.23 shows the dependence of the supercontinuum (mainly from the SPM contribution) signal intensity on salt concentration for aqueous solutions of K_2ZnCl_4 , ZnCl_2 , and KCl at 570 nm (Figure 2.23a) and 500 nm (Figure 2.23b). The data were normalized with respect to the average ultrafast supercontinuum signal intensity obtained from neat water. These data indicated that the supercontinuum pulse intensity was highly dependent on salt concentration and that both the Stokes and the anti-Stokes sides of the supercontinuum signals from a saturated K_2ZnCl_4 solution were about 10 times larger than from neat water. The insets in Figure 2.23 are the same data plotted as a function of K^+ ion concentration for KCl and K_2ZnCl_4 aqueous solutions. Solutions of KCl and K_2ZnCl_4 generate almost the same amount of supercontinuum if the K^+ cation concentration is same, even though they contain different amounts of Cl^- anions. This indicates that the Cl^- anion has little effect on generation of the supercontinuum. The Zn^{2+} cations also enhanced the supercontinuum, though to a lesser extent than the K^+ cations.

The measurements of the optical Kerr effect and the ultrafast supercontinuum in salt-saturated aqueous solutions are summarized in Table 2.3. The measured n_2 (pure H_2O) is about 220 times smaller than n_2 (CS_2). The value $G_{\text{SPM}}(\lambda)$ represents the ratio of the SPM signal intensity from a particular salt solution to that from neat water at wavelength λ . G_{Kerr} is defined as the ratio of the transmitted intensity caused by a polarization change of the probe beam in a particular salt solution to that in neat water; G_{Kerr} is equal to $[n_2(\text{particular solution})/n_2(\text{water})]^2$. Table 2.3 shows that, at saturation, K_2ZnCl_4

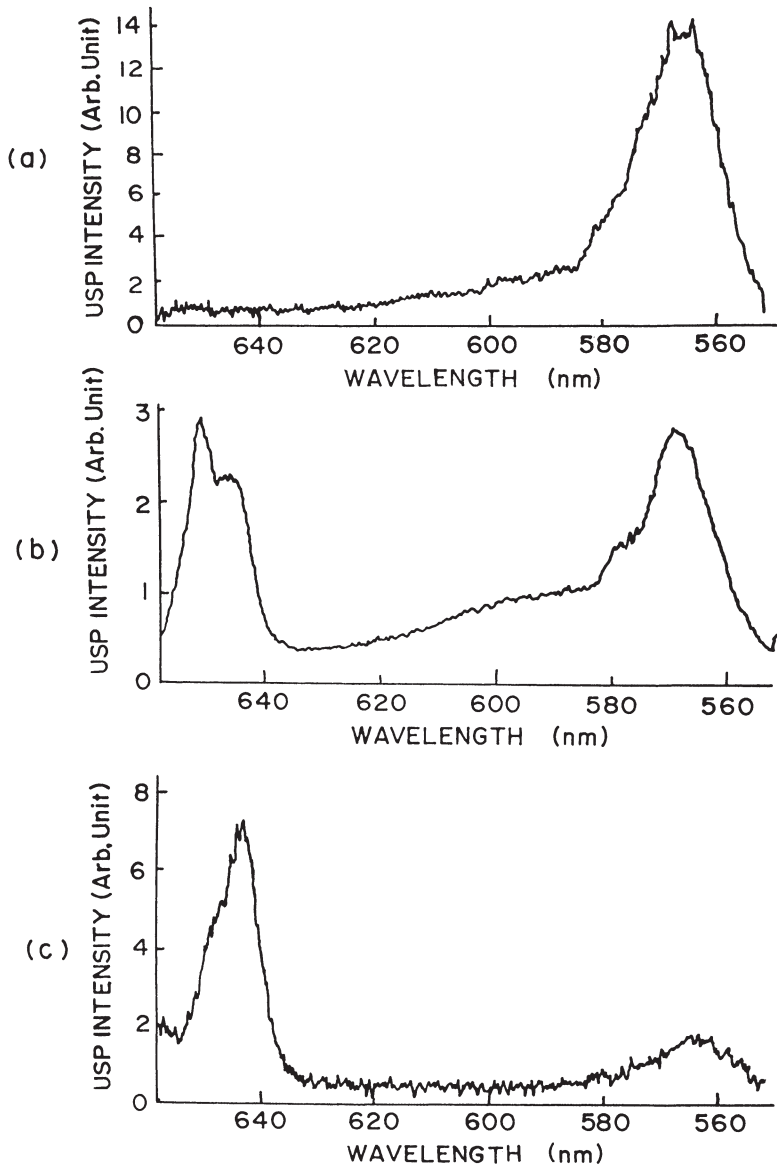


FIGURE 2.22. SPM spectrum of (a) saturated K_2ZnCl_4 solution, (b) 0.6-m K_2ZnCl_4 , and (c) pure water. The SRS signal (645 nm) is stronger in pure water, and it disappears in high-concentration solution. (From Jimbo et al., 1987.)

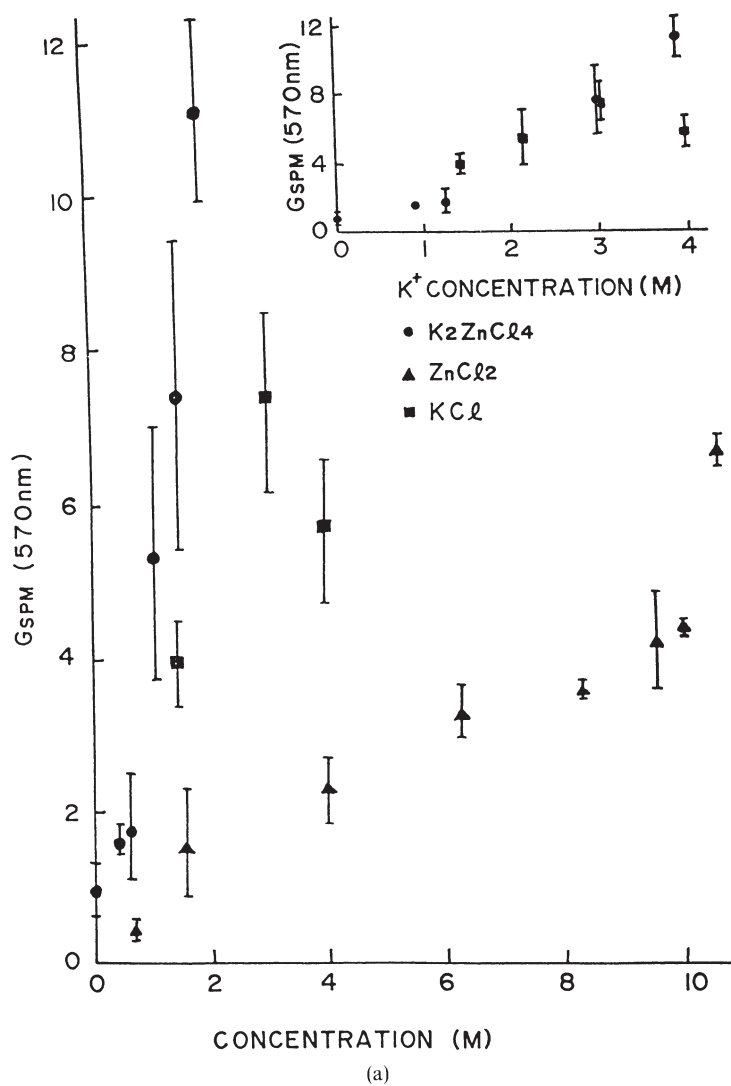


FIGURE 2.23. Salt concentration dependence of the SPM signal (a) on the Stokes side and (b) on the anti-Stokes side 20°C. Each data point is the average of about 10 laser shots. The inserts are the same data plotted as a function of K^+ ion concentration for KCl and K_2ZnCl_4 aqueous solutions. (From Jimbo et al., 1987.)

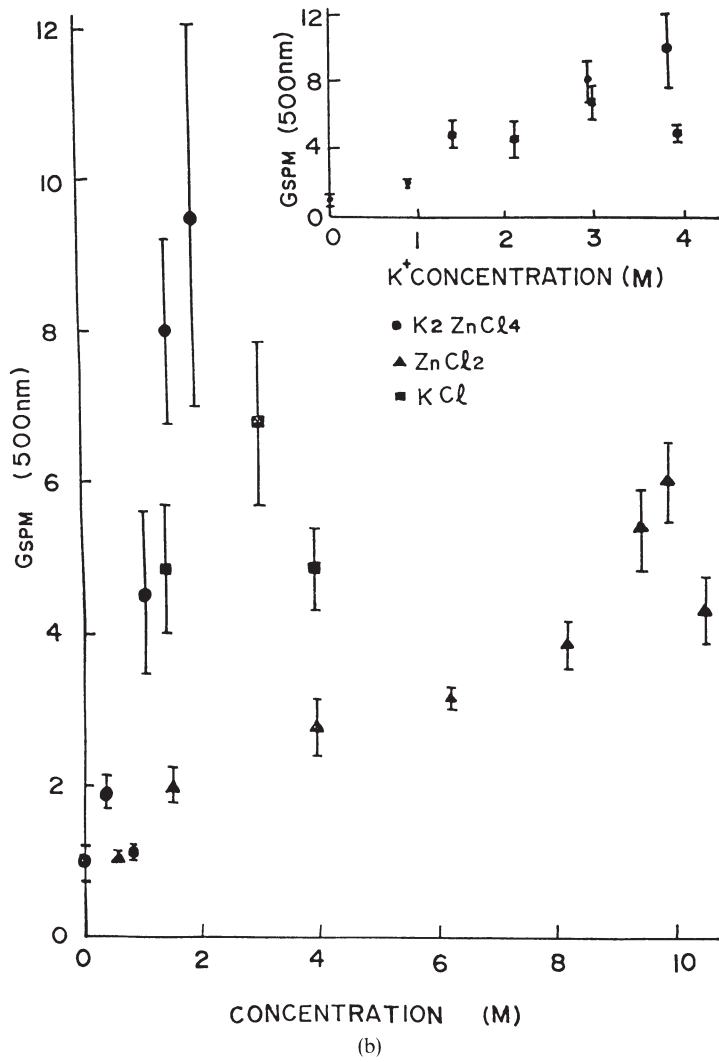


FIGURE 2.23. (continued)

TABLE 2.3. Enhancement of the supercontinuum and optical Kerr effects signals in saturated aqueous solutions at 20°C.^a

Signal	K ₂ ZnCl ₄ (1.9 M)	KCl (4.0 M)	ZnCl ₂ (10.6 M)
$G_{\text{SPM}}(570)$	11 ± 1	5.6 ± 0.9	6.6 ± 0.4
$G_{\text{SPM}}(500)$	9.5 ± 2.5	4.9 ± 0.2	4.3 ± 0.5
G_{Kerr}	16 ± 1	6.1 ± 1.4	35 ± 9

^a $G_{\text{SPM}}(\lambda) = [I_{\text{SPM}}(\lambda)/I_{\text{laser}}(530 \text{ nm})]_{\text{solution}}/[I_{\text{SPM}}(\lambda)/I_{\text{laser}}(530 \text{ nm})]_{\text{water}}$
and $G_{\text{Kerr}} = [I_{\text{Kerr}}(\text{solution})]/[I_{\text{Kerr}}(\text{water})]$.

produced the greatest increase in the supercontinuum. Although ZnCl₂ generated the largest enhancement of the optical Kerr effect, it did not play an important role in the enhancement of the ultrafast supercontinuum (a possible reason for this is discussed below). The optical Kerr effect signal from saturated solutions of ZnCl₂ was about 2 to 3 times greater than that from saturated solutions of K₂ZnCl₄.

The enhancement of the optical nonlinearity of water by the addition of cations can be explained by the cations' disruption of the tetrahedral hydrogen-bonded water structures and their formation of hydrated units (Walrafen, 1972). Since the nonlinear index n_2 is proportional to the number density of molecules, hydration increases the number density of water molecules and thereby increases n_2 . The ratio of the hydration numbers of Zn²⁺ and K⁺ has been estimated from measurements of G_{Kerr} and compared with their values based on ionic mobility measurements. At the same concentration of KCl and ZnCl₂ aqueous solution, $(G_{\text{Kerr}} \text{ generated by ZnCl}_2 \text{ solution})/(G_{\text{Kerr}} \text{ generated by KCl solution}) = [N(\text{Zn}^{2+})/N(\text{K}^+)]^2 \sim 2.6$, where $N(\text{Zn}^{2+}) \sim 11.2 \pm 1.3$ and $N(\text{K}^+) \sim 7 \pm 1$ represent the hydration numbers for the Zn²⁺ and K⁺ cations, respectively. The calculation of the hydration number of $N(\text{Zn}^{2+})/N(\text{K}^+) \sim 1.5$ is in good agreement with the Kerr non-linearity measurements displayed in Table 2.3.

In addition, from our previous measurements and discussions of nonlinear processes in mixed binary liquids (Ho and Alfano, 1978), the total optical nonlinearity of a mixture modeled from a generalized Langevin equation was determined by the coupled interactions of solute-solute, solute-solvent, and solvent-solvent molecules. The high salt solution concentration may contribute additional optical nonlinearity to the water owing to the distortion from the salt ions and the salt-water molecular interactions.

The finding that Zn²⁺ cations increased G_{Kerr} more than G_{SPM} is consistent with the hydration picture. The transmitted signal of the OKG depends on Δn , while the ultrafast supercontinuum signal is determined by $\partial n/\partial t$. The ultrafast supercontinuum also depends on the response time of the hydrated units. Since the Zn²⁺ hydrated units are larger than those of K⁺, the response time will be longer. These effects will be reduced for longer pulses. Two addi-

tional factors may contribute to part of the small discrepancy between G_{SPM} and G_{Kerr} for ZnCl_2 . The first one is related to the mechanism of δn generation in which χ_{1111} is involved in the generation of SPM while the difference $\chi_{1111} - \chi_{1112}$ is responsible for the optical Kerr effect. The second is the possible dispersion of n_2 because of the difference in wavelength between the exciting beams of the ultrafast supercontinuum and the optical Kerr effects.

The optical Kerr effect is enhanced 35 times by using ZnCl_2 as a solute, and the ultrafast supercontinuum is enhanced about 10 times by using K_2ZnCl_4 as a solute. The enhancement of the optical nonlinearity has been attributed to an increase in the number density of water molecules owing to hydration and the coupled interactions of solute and solvent molecules. Addition of ions can be used to increase n_2 for SPM generation and gating.

11. Temporal Behavior of SPM

In addition to spectral features, the temporal properties of the supercontinuum light source are important for understanding the generation and compression processes. In this section, the local generation, propagation, and pulse duration reduction of SPM are discussed.

11.1 Temporal Distribution of SPM

In Section 2, using the stationary phase method, it was described theoretically that the Stokes and anti-Stokes frequencies should appear at well-defined locations in time within leading and trailing edges of the pump pulse profile (Alfano, 1972). Theoretical analyses by Stolen and Lin (1978) and Yang and Shen (1984) obtained similar conclusions.

Passing an 80-fs laser pulse through a 500- μm -thick ethylene glycol jet stream, the pulse duration of the spectrum in time was measured by the autocorrelation method (Fork et al., 1983). These results supported the SPM mechanism for supercontinuum generation. In the following, the measurements of the distribution of various wavelengths for the supercontinuum generated in CCl_4 by intense 8-ps laser pulses (Li et al., 1986) are presented. Reduction of the pulse duration using the SPM principle is discussed in Section 10.3.

The incident 530-nm laser pulse temporal profile is shown in Figure 2.24. The pulse shape can be fitted with a Gaussian distribution with duration $\tau(\text{FWHM}) = 8\text{ ps}$. The spectral and temporal distributions of the supercontinuum pulse were obtained by measuring the time difference using a streak camera. The measured results are shown as circles in Figure 2.25. Each data point corresponds to an average of about six laser shots. The observation is consistent with the SPM and group velocity dispersion. To determine the temporal distribution of the wavelengths generated within a supercontinuum, the group velocity dispersion effect (Topp and Orner, 1975) in CCl_4

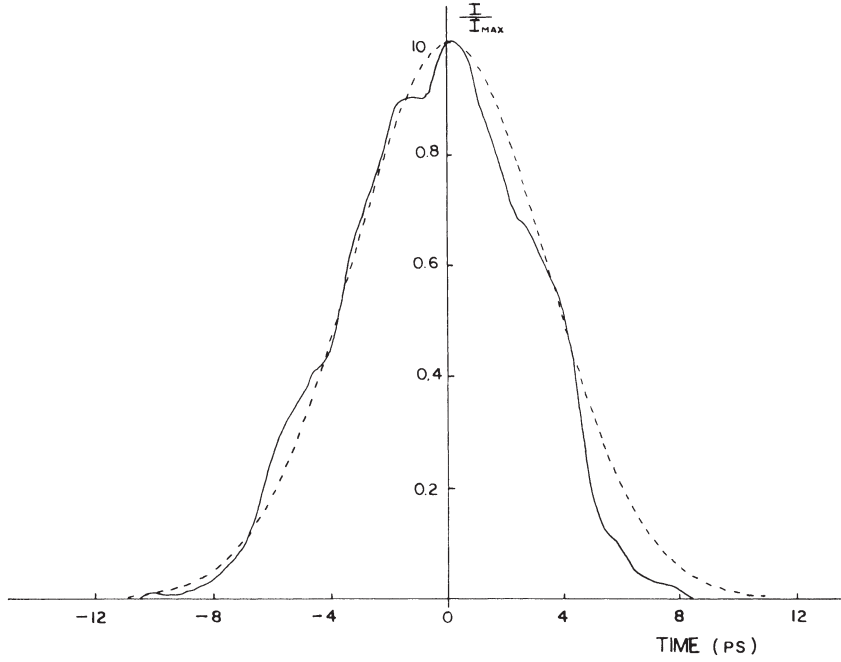


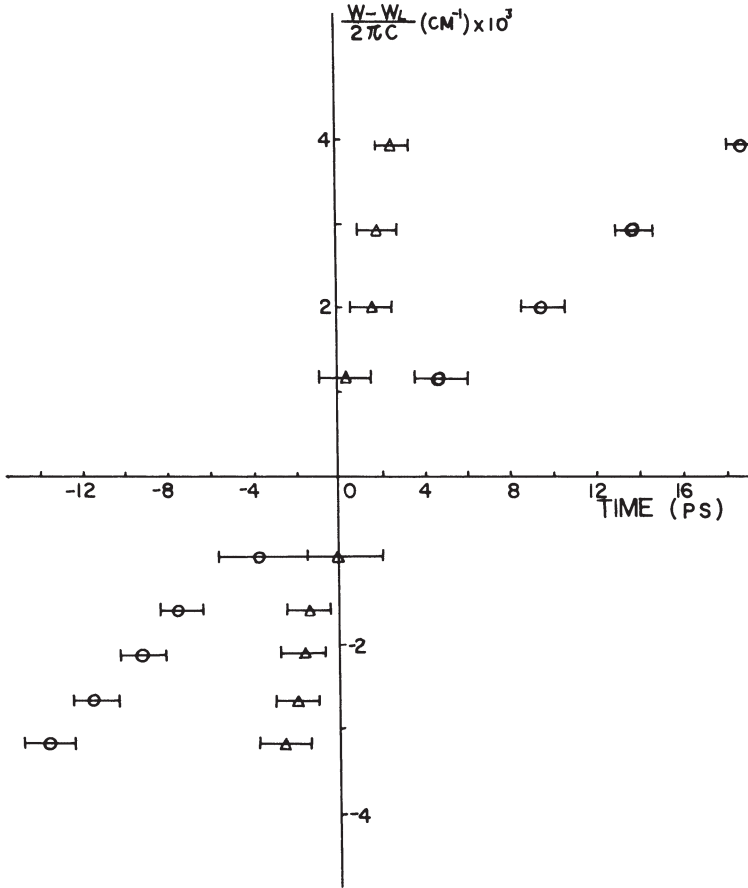
FIGURE 2.24. Temporal profile of a 530-nm incident laser pulse measured by a 2-ps-resolution streak camera. The dashed line is a theoretical fit to an 8-ps EWHM Gaussian pulse. (From Li et al., 1986.)

was corrected. Results corrected for both the optical delay in the added filters and the group velocity are displayed as triangles in Figure 2.25. The salient feature of Figure 2.25 indicates that the Stokes wavelengths of the continuum lead the anti-Stokes wavelengths.

Using the stationary phase SPM method [Eq. (6)], the generated instantaneous frequency ω of the supercontinuum can be expressed by

$$\omega(t) - \omega_L = -(\omega_L l / c) \partial(\Delta n) / \partial t, \quad (33)$$

where ω_L is the incident laser angular frequency, l is the length of the sample, and Δn is the induced nonlinear refractive index $n_2 E^2$. A theoretical calculated curve for the sweep is displayed in Figure 2.26 by choosing appropriate parameters to fit the experimental data of Figure 2.25. An excellent fit using a stationary phase model up to maximum sweep demonstrates that the generation mechanism of the temporal distribution of the supercontinuum arises from the SPM. During the SPM process, a wavelength occurs at a well-defined time within the pulse. The above analysis will be supported by the additional experimental evidence for SPM described in Section 10.3 (see Figure 2.29).



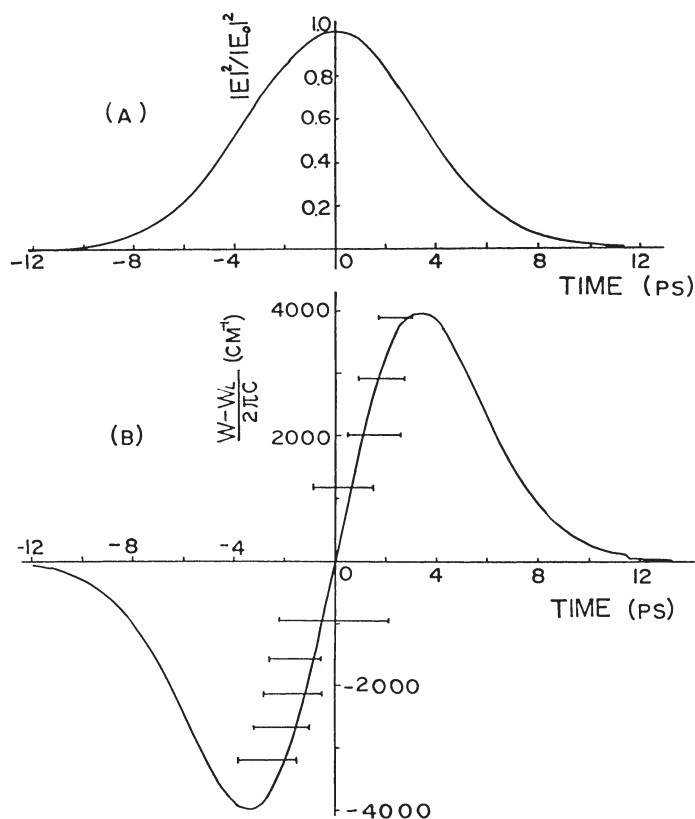


FIGURE 2.26. Comparison of the measured temporal distribution of supercontinuum with the SPM model. (From Li et al., 1986.)

Typical data on the time delay of 10-nm-bandwidth pulses centered at 530, 650, and 450 nm wavelengths of the supercontinuum generated from a 20-cm-long cell filled with CCl_4 are displayed in Figure 2.27. The peak locations of 530, 650, and 450 nm are -49, -63, and -30 ps, respectively. The salient features in Figure 2.27 (Ho et al., 1987) indicate that the duration of all 10-nm-band supercontinuum pulses is only 6 ps, which is shorter than the incident pulse of 8 ps, the Stokes side (650 nm) of the supercontinuum pulse travels ahead of the pumping 530 nm by 14 ps, and the anti-Stokes side (450 nm) of the supercontinuum pulse lags the 530 nm by 10 ps.

If the supercontinuum could be generated throughout the entire length of the sample, the Stokes side supercontinuum pulse generated by the 530-nm incident laser pulse at $z = 0$ cm of the sample would be ahead of the 530-nm incident pulse after propagating through the length of the sample. Over this path, 530 nm could continuously generate the supercontinuum pulse. Thus, the Stokes side supercontinuum generated at the end of the sample coincides in time with the 530-nm incident pulse. In this manner, a supercontinuum

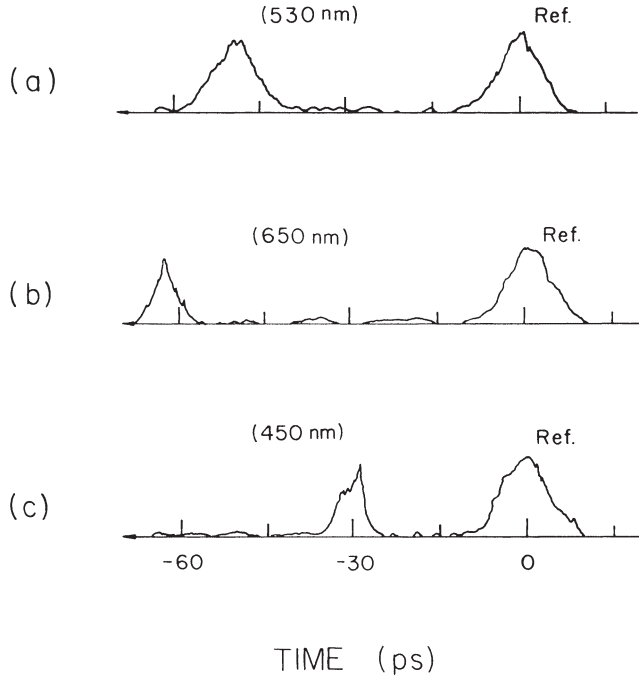


FIGURE 2.27. Temporal profiles and pulse locations of a selected 10-nm band of a supercontinuum pulse at different wavelengths propagated through a 20-cm-long CCl_4 cell: (a) $\lambda = 530$ nm; (b) $\lambda = 650$ nm; (c) $\lambda = 450$ nm. Filter effects were compensated. (From Ho et al., 1987.)

pulse centered at a particular Stokes frequency could have a pulse greater than the incident pulse extending in time from the emerging of the 530-nm pulse to the position where the Stokes frequency was originally produced at $z \sim 0$ cm. From a similar consideration, the anti-Stokes side supercontinuum pulse would also be broadened. However, no slow asymmetric tail for the Stokes pulse or rise for the anti-Stokes pulse is displayed in Figure 2.27. These observations suggest the local generation of supercontinuum pulses.

A model to describe the generation and propagation features of the supercontinuum pulse has been formulated based on local generation. The time delay of Stokes and anti-Stokes supercontinuum pulses relative to the 530-nm pump pulse is accounted for by the filaments formed ~ 5 cm from the sample cell entrance window. The 5-cm location is calculated from data in Figure 2.27 by using the equation.

$$T_{530} - T_{\text{supercon.}} = \Delta x \left(\frac{1}{v_{530}} - \frac{1}{v_{\text{supercon.}}} \right), \quad (34)$$

where Δx is the total length of supercontinuum pulse travel in CCl_4 after the generation. T_{530} and $T_{\text{supercon.}}$ are the 530-nm and supercontinuum pulse peak

time locations in Figure 2.27, and v_{530} and $v_{\text{supercon.}}$ are the group velocities of the 530-nm and supercontinuum pulses, respectively.

The duration of the supercontinuum pulse right at the generation location is either limited by the bandwidth of the measurement from the SPM process or shortened by the parametric generation process. In either cases, a 10-nm-bandwidth supercontinuum pulse will have a shorter duration than the incident pulse. After being generated, each of these 10-nm-bandwidth supercontinuum pulses will travel through the rest of the sample and will continuously generated by the incident 530 nm over a certain interaction length before these two pulses walk off. The interaction length can be calculated as (Alfano, 1972).

$$l = \tau \frac{v_{530} v_{\text{supercon.}}}{v_{530} - v_{\text{supercon.}}}, \quad (35)$$

where l is the interaction length over the pump and the supercontinuum pulses stay spatially coincident by less than the duration (FWHM) of the incident pump pulse, and τ is the duration of the supercontinuum pulse envelope. From Eq. (35), one can estimate the interaction length from the measured τ of the supercontinuum pulse. Using parameters $\tau = 6$ ps, $v_{530} = c/1.4868$, and $v_{\text{supercon.}} = c/1.4656$, the interaction length $l = 8.45$ cm is calculated. This length agrees well with the measured beam waist length of 8 cm for the pump pulse in CCl_4 .

Since no long tails were observed from the supercontinuum pulses to the dispersion delay times of the Stokes and anti-Stokes supercontinuum pulses, the supercontinuum was not generated over the entire length of 20 cm but only over 1 to 9 cm. This length is equivalent to the beam waist length of the laser in CCl_4 . The length of the local SPM generation over a distance of 8.45 cm yields a possible explanation for the 6-ps supercontinuum pulse duration. In addition, a pulse broadening of 0.3 ps calculated from the group velocity dispersion of a 10-nm band at 650-nm supercontinuum traveling over 20 cm of liquid CCl_4 is negligible in this case.

Therefore, the SPM pulses have shorter durations than the pump pulse and were generated over local spatial domains in the liquid cell.

11.3 SPM Pulse Duration Reduction

The principle behind the pulse narrowing based on the spectral temporal distribution of the SPM spectrally broadened in time within the pulse is described in Sections 2 and 10.1. At each time t within the pulse there is a frequency $\omega(t)$. When a pulse undergoes SPM, the changes in the optical carrier frequency within the temporal profile are greatest on the rising and falling edges, where the frequency is decreased and increased, respectively. Near the peak of the profile, and in the far leading and trailing wings, the carrier frequency structure is essentially unchanged. The maximum frequency shift is proportional to the intensity gradient on the sides of the pulse, and

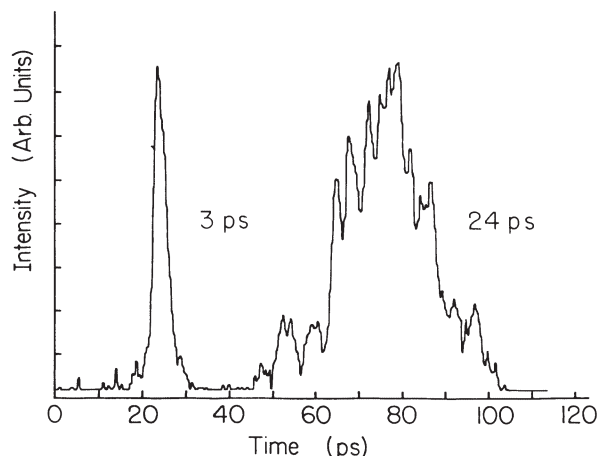


FIGURE 2.28. Streak camera temporal profile of the 25-ps, 530-nm incident laser pulse and 10-nm-bandwidth pulse at 580 nm. The 3-ps pulse was obtained by spectral filtering a SPM frequency continuum generated in D_2O . (From Dorsinville et al., 1987.)

this determines the position of the outer lobes of the power spectrum. If these are then attenuated by a spectral window of suitably chosen width, the wings of the profile where the high- and low-frequency components are chiefly concentrated will be depressed, while the central peak will be largely unaffected. The overall effect is to create a pulse that is significantly narrower in time than the original pulse duration. A filter can be used to select a narrow portion of the pulse, giving rise to a narrower pulse in time.

A threefold shortening of 80-ps pulses to 30 ps from an Nd:YAG laser broadened from 0.3 to 4 Å after propagation through 125 m of optical fiber with a monochromator as a spectral window was demonstrated using this technique (Gomes et al., 1986). The measurements of pulses at different wavelengths of the frequency sweep of supercontinuum pulses generated by 8-ps laser pulses propagating in CCl_4 show that the continuum pulses have a shorter duration (~6 ps) than the pumping pulses (Li et al., 1986).

A major advance occurred when a 25-ps laser pulse was focused into a 5-cm-long cell filled with D_2O . A continuum was produced. Using 10-nm-bandwidth narrowband filters, tunable pulses of less than 3 ps in the spectral range from 480 to 590 nm (Figure 2.28) were produced (Dorsinville et al., 1987).

To identify the SPM generation mechanism, the temporal distribution of the continuum spectrum was determined by measuring the time delay between the continuum and a reference beam at different wavelengths using a streak camera. The results are displayed in Figure 2.29, which is similar to data displayed in Figure 2.25. The time delay was ~22 ps for a 140-nm change in wavelength; as predicted by the SPM mechanism, the Stokes wavelength led the anti-Stokes wavelength (Alfano, 1972). The delay due to group velocity over a 5-cm D_2O cell for the 140-nm wavelength change is less than 3 ps.

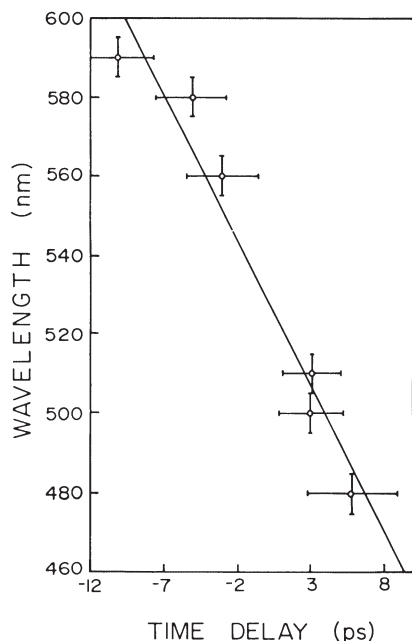


FIGURE 2.29. Continuum temporal distribution at different wavelengths. Horizontal error bars correspond to 10-nm band-widths of the filter. (From Dorsinville et al., 1987.)

The remaining 18 ps is well accounted for by the SPM mechanism using a 25-ps (FWHM) pulse and the stationary phase method (Alfano, 1972). Furthermore, a 10-nm selected region in the temporal distribution curve corresponds to an ~ 2.6 -ps width matching the measured pulse duration (Figure 2.28). This observation suggests that by using narrower bandwidth filters the pulse duration can be shortened to the uncertainty limit.

12. Higher-Order Effects on Self-Phase Modulation

A complete description of SPM-generated spectral broadening should take into account higher-order effects such as self-focusing, group velocity dispersion, self-steepening, and initial pulse chirping. Some of these effects are described by Suydam (Chapter 6), Shen (Chapter 1), and Agrawal (Chapter 3). These effects will influence the observed spectral profiles.

12.1 Self-Focusing

In the earliest experiments using picosecond pulses, the supercontinuum pulses were often generated in small-scale filaments resulting from the self-focusing of intense laser beams (Alfano, 1972). Self-focusing arises from the radial dependence of the nonlinear refractive index $n(r) = n_0 + n_2 E^2(r)$ (Shen, 1984; Auston, 1977). It has been observed in many liquids, bulk materials (Shen, 1984), and optical fibers (Baldeck et al., 1987a). Its effects on the continuum pulse generation can be viewed as good and bad. On the one hand,

it facilitates the spectral broadening by concentrating the laser beam energy. On the other hand, self-focusing is a random and unstable phenomenon that is not controllable. Femtosecond supercontinua are generated with thinner samples than picosecond supercontinua, so it can reduce but not totally eliminate self-focusing effects.

12.2 Dispersion

Group velocity dispersion (GVD) arises from the frequency dependence of the refractive index. These effects are described by Agrawal (Chapter 3). The first-order GVD term leads to a symmetric temporal broadening (Marcuse, 1980). A typical value for the broadening rate arising from $\partial^2 k / \partial \omega^2$ is 500 fs/m · nm (in silica at 532 nm). In the case of supercontinuum generation, spectral widths are generally large (several hundred nanometers), but interaction lengths are usually small (<1 cm). Therefore, the temporal broadening arising from GVD is often negligible for picosecond pulses but is important for femtosecond pulses. Limitations on the spectral extent of supercontinuum generation are also related to GVD. Although the spectral broadening should increase linearly with the medium length (i.e., $\Delta\omega(z)_{\max} = \omega_0 n_2 a^2 z / c \Delta\tau$), it quickly reaches a maximum as shown in Figure 2.10. This is because GVD, which is large for pulses having SPM-broadened spectra, reduces the pulse peak power a^2 and broadens the pulse duration $\Delta\tau$. As shown in Figure 2.25, the linear chirp parameter is decreased by the GVD chirp in the normal dispersion regime. This effect is used to linearize chirp in the pulse compression technique.

The second-order term $\partial^3 k / \partial \omega^3$ has been found to be responsible for asymmetric distortion of temporal shapes and modulation of pulse propagation in the lower region of the optical fiber (Agrawal and Potasek, 1986). Since the spectra of supercontinuum pulses are exceptionally broad, this term should also lead to asymmetric distortions of temporal and spectral shapes of supercontinuum pulses generated in thick samples. These effects have been observed.

In multimode optical fibers, the mode dispersion dominates and causes distortion of the temporal shapes. This in turn yields asymmetric spectral broadening (Wang et al., 1988).

12.3 Self-Steepening

Pulse shapes and spectra of intense supercontinuum pulses have been found to be asymmetric (De Martini et al., 1967). There are two potential sources of asymmetric broadening in supercontinuum generation. The first one is the second-order GVD term. The second one is self-steepening, which is intrinsic to the SPM process and occurs even in nondispersion media. Details of the effects of self-steepening can be found in Suydam (Chapter 6), Shen and Yang (Chapter 1), and Manassah (Chapter 5).

Because of the intensity and time dependence of the refractive index, $n = n_0 + n_2 E(t)^2$, the supercontinuum pulse peak sees a higher refractive index than its edges. Because $v = c/n$, the pulse peak travels slower than the leading and

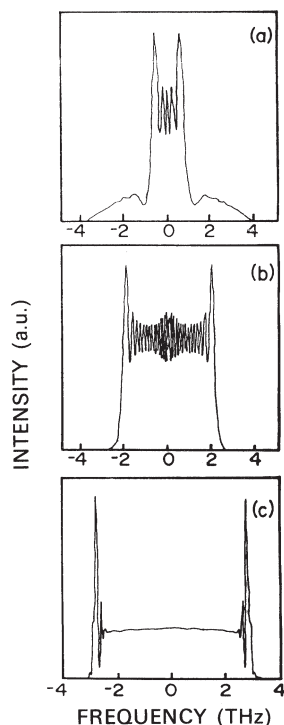


FIGURE 2.30. Influence of initial pulse chirping on SPM-broadened spectra in optical fibers. Peak power = 1000 W. (a) $C = 50$; (b) $C = 0$; (c) $C = -50$ [see Eq. (17)]. (From Baldeck et al., 1987b.)

trailing edges. This results in a sharpened trailing edge. Self-steepening occurs and more blue-shifted frequencies (sharp trailing edge) are generated than red frequencies. Several theoretical approaches have given approximate solutions for the electric field envelope distorted by self-steepening and asymmetric spectral extent. Actual self-steepening effects have not been observed in the time domain.

12.4 Initial Pulse Chirping

Most femtosecond and picosecond pulses are generated with initial chirps. Chirps arise mainly from GVD and SPM in the laser cavity. As shown in Figure 2.30, the spectral broadening is reduced for positive chirps and enhanced for negative chirps in the normal dispersion regime. The spectral distribution of SPM is also affected by the initial chirp.

13. Overview

Supercontinuum generation is the generation of bursts of “white” light, which can be obtained by passing intense picosecond or femtosecond pulses through various materials. Because of the nonlinear response of the medium,

the pulse envelope yields a phase modulation that initiates the wide frequency broadening (up to $10,000\text{ cm}^{-1}$). The phase modulation can be generated by the pulse itself, a copropagating pump pulse, or the copropagating stronger pulse. These different configurations are called self-phase modulation (SPM), induced-phase modulation (IPM), and cross-phase modulation (XPM), respectively. The SPM process for supercontinuum generation in various materials was reviewed in this chapter. This latter two processes are closely related to each other and are described by Baldeck et al. (Chapter 4), Agrawal (Chapter 3), and Manassah (Chapter 5).

Using an 8-ps laser at 530 nm, typical Stokes sweeps were 4400 cm^{-1} in a calcite crystal of length 4 cm, 3900 cm^{-1} in a quartz crystal of length 4.5 cm, 1100 cm^{-1} in extra-dense flint glass of length 7.55 cm, 3900 cm^{-1} in NaCl of length 4.7 cm, and 4200 cm^{-1} in both BK-7 and LBC-1 glasses of length 8.9 cm. Sweeps on the anti-Stokes side were typically 6100 cm^{-1} in calcite, 5500 cm^{-1} in quartz, 7300 cm^{-1} in NaCl, and 7400 cm^{-1} in BK-7 and LBC-1 glasses. An infrared supercontinuum spanning the range from 3 to $14\text{ }\mu\text{m}$ can be obtained by passing an intense laser pulse generated from a CO_2 laser through GaAs, AgBr, ZnSe, and CdS crystals. Near- and medium-infrared spectral sweeps of 3200 cm^{-1} on the Stokes side and 4900 cm^{-1} on the anti-Stokes side can be realized by passing a strong $1.06\text{-}\mu\text{m}$ pulse through a KBr crystal of length 10 cm. Sweeps on the order of 1000 cm^{-1} are observed to both the red and blue sides of 530 nm in liquid argon. Similar spectral sweeps are observed in liquid and solid krypton arising from electronic mechanism for SPM. Using a picosecond laser train of wavelength 530 nm, the spectra were broadened up to 3000 cm^{-1} to either side of the laser frequency in a 5-cm-long magnetic KNiF_3 single crystal. Production of SPM near electronic levels of PrF_3 crystal and enhancement of supercontinuum in water by addition of Zn^{2+} and K^+ cations have been also discussed. The temporal properties of supercontinuum pulses have been described. Higher-order effects on SPM arising from dispersion, self-focusing, self-steepening, and initial pulse chirping were briefly described.

SPM will continue to be an important nonlinear process in science and technology and has been one of the most important ultrafast nonlinear optical processes for more than 20 years since the advent of ultrashort laser pulses!

References

- Agrawal, G.P. and M.J. Potasek (1986) Nonlinear pulse distortion in single-mode optical fibers at the zero-dispersion wavelength. *Phys. Rev. A* **33**, 1765–1776.
- Alfano, R.R. (1972) Interaction of picosecond laser pulses with matter. GTE Technical Report TR 72–330. Published as Ph.D. thesis at New York University, 1972.
- Alfano, R.R. (1986) The ultrafast supercontinuum laser source. *Proc. International Conference Laser '85*. STS Press, McLean, Virginia, pp. 110–122.
- Alfano, R.R. and P.P. Ho (1988) Self-, cross-, and induced-phase modulations of ultrashort laser pulse propagation. *IEEE J. Quantum Electron.* **QE-24**, 351–363.

- Alfano, R.R. and S.L. Shapiro (1970a) Emission in the region 4000–7000 Å via four-photon coupling in glass. *Phys. Rev. Lett.* **24**, 584–587; Observation of self-phase modulation and small scale filaments in crystals and glasses. *Phys. Rev. Lett.* **24**, 592–594; Direct distortion of electronic clouds of rare-gas atoms in intense electric fields. *Phys. Rev. Lett.* **24**, 1219–1222.
- Alfano, R.R. and S.L. Shapiro (1970b) Picosecond spectroscopy using the inverse Raman effect. *Chem. Phys. Lett.* **8**, 631–633.
- Alfano, R.R., L. Hope, and S. Shapiro (1972) Electronic mechanism for production of self-phase modulation. *Phys. Rev. A* **6**, 433–438.
- Alfano, R.R., J. Gersten, G. Zawadzka, and N. Tzoar (1974) Self-phase-modulation near the electronic resonances of a crystal. *Phys. Rev. A* **10**, 698–708.
- Alfano, R.R., P. Ho, P. Fleury, and H. Guggenheim (1976) Nonlinear optical effects in antiferromagnetic KNiF_3 . *Opt. Commun.* **19**, 261–264.
- Alfano, R.R., Q. Li, T. Jimbo, J. Manassah, and P. Ho (1986) Induced spectral broadening of a weak picosecond pulse in glass produced by an intense ps pulse. *Opt. Lett.* **11**, 626–628.
- Alfano, R.R., Q.Z. Wang, T. Jimbo, and P.P. Ho (1987) Induced spectral broadening about a second harmonic generated by an intense primary ultrashort laser pulse in ZnSe crystals. *Phys. Rev. A* **35**, 459–462.
- Alfano, R.R., Q.Z. Wang, D. Ji, and P.P. Ho (1989) Harmonic cross-phase-modulation in ZnSe. *App. Phys. Lett.* **54**, 111–113.
- Anderson, D. and M. Lisak (1983) Nonlinear asymmetric self-phase modulation and self-steepening of pulses in long optical waveguides. *Phys. Rev. A* **27**, 1393–1398.
- Auston, D.H. (1977) In *Ultrafast Light Pulses*, S.L. Shapiro, ed., Springer, Verlag, New York.
- Baldeck, P.L., F. Raccach, and R.R. Alfano (1987a) Observation of self-focusing in optical fibers with picosecond pulses. *Opt. Lett.* **12**, 588–589.
- Baldeck, P.L., P.P. Ho, and R.R. Alfano (1987b) Effects of self-, induced-, and cross-phase modulations on the generation of ps and fs white light supercontinuum. *Rev. Phys. Appl.* **22**, 1877–1894.
- Bloembergen, N. and P. Lallemand (1966) Complex intensity dependent index of refraction frequency broadening of stimulated Raman lines and stimulated Rayleigh scattering. *Phys. Rev. Lett.* **16**, 81–84.
- Bourkoff, E., W. Zhao, and R.I. Joseph (1987) Evolution of femtosecond pulses in single-mode fibers having higher-order nonlinearity and dispersion. *Opt. Lett.* **12**, 272–274.
- Brewer, R.G. (1967) Frequency shifts in self-focused light. *Phys. Rev. Lett.* **19**, 8–10.
- Brewer, R.G. and C.H. Lee (1968) Self-trapping with picosecond light pulses. *Phys. Rev. Lett.* **21**, 267–270.
- Busch, G.E., R.P. Jones, and P.M. Rentzepis (1973) Picosecond spectroscopy using a picosecond continuum. *Chem. Phys. Lett.* **18**, 178–185.
- Chinn, S.R., H. Zeiger, and J. O'Connor (1971) Two-magnon Raman scattering and exchange interactions in antiferromagnetic KNiF_3 and K_2NiF_4 and ferrimagnetic RbNiF_3 . *Phys. Rev.* **B3**, 1709–1735.
- Corkum, P., P. Ho, R. Alfano, and J. Manassah (1985) Generation of infrared supercontinuum covering 3–14 μm in dielectrics and semiconductors. *Opt. Lett.* **10**, 624–626.
- Corkum, P.B., C. Rolland, and T. Rao (1986) Supercontinuum generation in gases. *Phys. Rev. Lett.* **57**, 2268–2271.

- Cornelius, P. and L. Harris (1981) Role of self-phase modulation in stimulated Raman scattering from more than one mode. *Opt. Lett.* **6**, 129–131.
- DeMartini, F., C.H. Townes, T.K. Gustafson, and P.L. Kelly (1967) Self-steepening of light pulses. *Phys. Rev.* **164**, 312–322.
- Dorsinville, R., P. Delfyett, and R.R. Alfano (1987) Generation of 3 ps pulses by spectral selection of the supercontinuum generated by a 30 ps second harmonic Nd: YAG laser pulse in a liquid. *Appl. Opt.* **27**, 16–18.
- Fisher, R.A. and W. Bischel (1975) Numerical studies of the interplay wave laser pulse. *J. Appl. Phys.* **46**, 4921–4934.
- Fisher, R.A., B. Suydam, and D. Yevich (1983) Optical phase conjugation for time domain undoing of dispersion self-phase modulation effects. *Opt. Lett.* **8**, 611–613.
- Fleury, P.A., W. Hayes, and H.J. Guggenheim (1975) Magnetic scattering of light in $\text{K}(\text{NiMg})\text{F}_3$. *J. Phys. C: Solid State* **8**, 2183–2189.
- Fork, R.L., C.V. Shank, C. Hirliman, R. Yen, and J. Tomlinson (1983) Femtosecond white-light continuum pulse. *Opt. Lett.* **8**, 1–3.
- Fork, R.L., C.H. Brito Cruz, P.C. Becker, and C.V. Shank (1987) Compression of optical pulses to six femtoseconds by using cubic phase compensation. *Opt. Lett.* **12**, 483–485.
- Gersten, J., R. Alfano, and M. Belic (1980) Combined stimulated Raman scattering in fibers. *Phys. Rev. A* **21**, 1222–1224.
- Girodmaine, J.A. (1962) Mixing of light beams in crystals. *Phys. Rev. Lett.* **8**, 19–20.
- Glownia, J., G. Arjavalingam, P. Sorokin, and J. Rothenberg (1986) Amplification of 350-fs pulses in XeCl excimer gain modules. *Opt. Lett.* **11**, 79–81.
- Goldberg, L. (1982) Broadband CARS probe using the picosecond continua. In *Ultrafast Phenomena III*. Springer-Verlag, New York, pp. 94–97.
- Gomes, A.S.L., A.S. Gouveia-Neto, J.R. Taylor, H. Avramopoulos, and G.H.C. New (1986) Optical pulse narrowing by the spectral windowing of self-phase modulated picosecond pulses. *Opt. Commun.* **59**, 399.
- Gustafson, T.K., I.P. Taran, H.A. Haus, J.R. Lifisitz, and P.L. Kelly (1969) Self-modulation, self-steepening, and spectral development of light in small-scale trapped filaments. *Phys. Rev.* **177**, 306–313.
- Gustafson, T.K., J. Taran, P. Kelley, and R. Chiao (1970) Self-modulation of picosecond pulse in electro-optical crystals. *Opt. Commun.* **2**, 17–21.
- Hellwarth, R.W. (1970) Theory of molecular light scattering spectra using linear-dipole approximation. *J. Chem. Phys.* **52**, 2128–2138.
- Hellwarth, R.W., J. Cherlow, and T.T. Yang (1975) Origin and frequency dependence of nonlinear optical susceptibilities of glasses. *Phys. Rev. B* **11**, 964–967.
- Heritage, J., A. Weiner, and P. Thurston (1985) Picosecond pulse shaping by spectral phase and amplitude manipulation. *Opt. Lett.* **10**, 609–611.
- Ho, P.P. and R.R. Alfano (1978) Coupled molecular reorientational relaxation kinetics in mixed binary liquids directly measured by picosecond laser techniques. *J. Chem. Phys.* **68**, 4551–4563.
- Ho, P.P. and R.R. Alfano (1979) Optical Kerr effect in liquids. *Phys. Rev. A* **20**, 2170–4564.
- Ho, P.P., Q.X. Li, T. Jimbo, Y.L. Ku, and R.R. Alfano (1987) Supercontinuum pulse generation and propagation in a liquid carbon tetrachloride. *Appl. Opt.* **26**, 2700–2702.
- Ishida, Y., K. Naganuma, T. Yagima, and C. Lin (1984) Ultrafast self-phase modulation in a colliding pulse mode-locking ring dye laser. In *Ultrafast Phenomena IV*. Springer-Verlag, New York, pp. 69–71.

- Jimbo, T., V.L. Caplan, Q.X. Li, Q.Z. Wang, P.P. Ho, and R.R. Alfano (1987) Enhancement of ultrafast supercontinuum generation in water by addition of Zn^{2+} and K^+ cations. *Opt. Lett.* **12**, 477–479.
- Johnson, A., R. Stolen, and W. Simpson (1986) The observation of chirped stimulated Raman scattering light in fibers. In *Ultrafast Phenomena* V.G.R. Fleming and A.E. Siegman ed. Springer-Verlag, New York, pp. 160–163.
- Jones, W.J. and B.P. Stoicheff (1964) Inverse Raman spectra: induced absorption at optical frequencies. *Phys. Rev. Lett.* **13**, 657–659.
- Knox, K., R.G. Shulman, and S. Sugano (1963) Covalency effects in KNiF_3 . II. Optical studies. *Phys. Rev.* **130**, 512–516.
- Knox, W., R. Fork, M. Dower, R. Stolen, and C. Shank (1985) Optical pulse compression to 8-fs at 5-kHz repetition rate. *Appl. Phys. Lett.* **46**, 1120–1121.
- Kobayashi, T. (1979) Broadband picosecond light generation in phosphoric acid by a mode-locked laser. *Opt. Commun.* **28**, 147–149.
- Lallemant, P. (1966) Temperature variation of the width of stimulated Raman lines in liquids. *Appl. Phys. Lett.* **8**, 276–277.
- Levenson, M.D. and N. Bloembergen (1974) Dispersion of the nonlinear optical susceptibility tensor in centrosymmetric media. *Phys. Rev. B* **10**, 4447–4463.
- L, Q.X., T. Jimbo, P.P. Ho, and R.R. Alfano (1986) Temporal distribution of picosecond super-continuum generated in a liquid measured by a streak camera. *Appl. Opt.* **25**, 1869–1871.
- Lozobkin, V., A. Malytin, and A. Prohorov (1970) Phase self-modulation of Nd: glass radiation with mode-locking. *JETP Lett.* **12**, 150–152.
- Magde, D. and M.W. Windsor (1974) Picosecond flash photolysis and spectroscopy: 3,3'-diethyloxadicarbocyanine iodide (DODCI). *Chem. Phys. Lett.* **27**, 31–36.
- Manassah, J.T., P.P. Ho, A. Katz, and R.R. Alfano (1984) Ultrafast supercontinuum laser source. *Photonics Spectra* **18** November, 53–59.
- Manassah, J.T., R.R., Alfano and M. Mustafa (1985a) Spectral distribution of an ultrashort supercontinuum laser source. *Phys. Lett. A* **107**, 305–309.
- Manassah, J.T., M. Mustafa, R. Alfano, and P. Ho (1985b) Induced supercontinuum and steepening of an ultrafast laser pulse. *Phys. Lett.* **113A**, 242–247.
- Manassah, J.T., M. Mustafa, R.R. Alfano, and P.P. Ho (1986) Spectral extent and pulse shape of the supercontinuum for ultrashort laser pulse. *IEEE J. Quantum Electron.* **QE-22**, 197–204.
- Marcuse, D. (1980) Pulse distortion in single-mode optical fibers *Appl. Opt.* **19**, 1653–1660.
- Masuhara, H., H. Miyasaka, A. Karen, N. Mataga, and Y. Tsuchiya (1983) Temporal characteristics of picosecond continuum as revealed by two-dimensional analysis of streak images. *Opt. Commun.* **4**, 426.
- McTague, J., P., Fleury, and D. DuPre (1969) Intermolecular light scattering in liquids. *Phys. Rev.* **188**, 303–308.
- Nakashima, N. and N. Mataga (1975) Picosecond flash photolysis and transient spectral measurements over the entire visible, near ultraviolet and near infrared regions. *Chem. Phys. Lett.* **35**, 487–492.
- Patel, C.K.N. and E.D. Shaw (1971) Tunable stimulated Raman scattering from mobile carriers in semiconductors. *Phys. Rev. B* **3**, 1279–1295.
- Penzokfer, A., A. Laubereau, and W. Kasier (1973) Stimulated short-wave radiation due to single frequency resonances of $\chi^{(3)}$. *Phys. Rev. Lett.* **31** 863–866.

- Potasek, M.J., G.P. Agrawal, and S.C. Pinault (1986) Analytical and numerical study of pulse broadening in nonlinear dispersive optical fibers. *J. Opt. Soc. Am.* **B 3**, 205–211.
- Shank, C. (1983) Measurement of ultrafast phenomena in the femtosecond domain. *Science* **219**, 1027.
- Shank, C.V., R.L. Fork, R. Yen, and R.H. Stolen (1982) Compression of femtosecond optical pulses. *Appl. Phys. Lett.* **40**, 761–763.
- Sharma, D.K., R.W. Yid, D.F. Williams, S.E. Sugamori, and L.L.T. Bradley (1976) Generation of an intense picosecond continuum in D₂O by a single picosecond 1.06 μ pulse. *Chem. Phys. Lett.* **41**, 460–465.
- Shen, Y.R. (1966) Electrostriction, optical Kerr effect and self-focusing of laser beams. *Phys. Lett.* **20**, 378.
- Shen Y.R. (1984) *The Principles of Nonlinear Optics*. Wiley, New York.
- Shimizu, F. (1967) Frequency broadening in liquids by a short light pulse. *Phys. Rev. Lett.* **19**, 1097–1100.
- Stolen, R.H. and A.M. Johnson (1986) The effect of pulse walkoff on stimulated Raman scattering in optical fibers. *IEEE J. Quantum Electron.* **QE-22**, 2154–2160.
- Stolen, R.H. and C. Lin (1978) Self-phase modulation in silica optical fibers. *Phys. Rev. A* **17**, 1448–1453.
- Topp, M.R. and G.C. Orner (1975) Group velocity dispersion effects in picosecond spectroscopy. *Opt. Commun.* **13**, 276.
- Tzoar, N. and M. Jain (1981) Self-phase modulation in long-geometry waveguide. *Phys. Rev. A* **23**, 1266–1270.
- Walrafen, G.E. (1972) Stimulated Raman scattering and the mixture model of water structure. *Adv. Mol. Relaxation Processes* **3**, 43–49.
- Wang, Q.Z., D. Ji, Lina Yang, P.P. Ho, and R.R. Alfano (1989) Self-phase modulation in multimode optical fibers with modest high power. Produced by moderately high power picosecond pulses. *Opt. Lett.*, in press.
- Yablonovitch, E. and N. Bloembergen (1972) Avalanche ionization of the limiting diameter of filaments induced by light pulses in transparent media. *Phys. Rev. Lett.* **29**, 907–910.
- Yang, G. and Y.R. Shen (1984) Spectral broadening of ultrashort pulse in a nonlinear medium. *Opt. Lett.* **9**, 510–512.
- Yu, W., R. Alfano, C.L. Sam, and R.J. Seymour (1975) Spectral broadening of picosecond 1.06 μ m pulse in KBr. *Opt. Commun.* **14**, 344.

Appendix: Nonlinear Wave Equation with Group Velocity Dispersion

We start with Maxwell equations for the electric and magnetic fields \mathbf{E} and \mathbf{H} in Gaussian units

$$\begin{aligned}
 \nabla \times \mathbf{E} &= -\frac{1}{c} \frac{\partial \mathbf{B}}{\partial t}, \\
 \nabla \times \mathbf{H} &= \frac{1}{c} \frac{\partial \mathbf{D}}{\partial t} + \frac{4\pi}{c} \mathbf{J}, \\
 \nabla \cdot \mathbf{D} &= 4\pi\rho, \\
 \nabla \cdot \mathbf{B} &= 0.
 \end{aligned}
 \tag{A.1}$$

The helping equations are $\mathbf{D} = \epsilon \mathbf{E}$ and $\mathbf{B} = \mu \mathbf{H}$, and \mathbf{J} and ρ are the current and charge densities, respectively. For nonmagnetic material, $\mathbf{B} \approx \mathbf{H}$. The refractive index of an isotropic material possessing nonlinearity can be written as

$$n(\omega) = [\epsilon(\omega)]^{1/2} = n_0(\omega) + n_2 |\mathbf{E}|^2, \quad (\text{A.2})$$

where $n_0(\omega)$ is the linear refractive index and n_2 the nonlinear refractive index. In the absence of sources, from Maxwell equations one can readily obtain the wave equation

$$\nabla^2 \mathbf{E}(\mathbf{r}, t) - \frac{1}{c^2} \frac{\partial^2}{\partial t^2} \mathbf{D}_L(\mathbf{r}, t) = \frac{2n_0 n_2}{c^2} \frac{\partial^2}{\partial t^2} (|\mathbf{E}|^2 \mathbf{E}(\mathbf{r}, t)), \quad (\text{A.3})$$

where $\mathbf{D}_L(\mathbf{r}, t)$ is the linear electric displacement vector. In obtaining the equation, we have used $\nabla \times (\nabla \times \mathbf{E}) = \nabla(\nabla \cdot \mathbf{E}) - \nabla^2 \mathbf{E} \approx -\nabla^2 \mathbf{E}$ and neglected the $(n_2)^2$ term.

The electric field can be written as

$$\mathbf{E}(\mathbf{r}, t) = \Phi(x, y) \mathbf{E}(z, t), \quad (\text{A.4})$$

where $\Phi(x, y)$ is the transverse distribution function. Substitute Eq. (A.4) into the wave equation and averaging over transverse coordinates, we have

$$\frac{\partial^2}{\partial z^2} \mathbf{E}(z, t) - \frac{1}{c} \frac{\partial^2}{\partial t^2} \mathbf{D}_L(z, t) = \frac{2n_0 \bar{n}_2}{c^2} \frac{\partial^2}{\partial t^2} |\mathbf{E}(z, t)|^2 \mathbf{E}(z, t). \quad (\text{A.5})$$

We have neglected the $\partial^2/\partial x^2$ and $\partial^2/\partial y^2$ terms. The effective nonlinear refractive index \bar{n}_2 is

$$\bar{n}_2 = \frac{\int n_2 \Phi^2(x, y) dx dy}{\int \Phi^2(x, y) dx dy} \approx \frac{1}{2} n_2. \quad (\text{A.6})$$

Using a plane wave approximation with $(k_0 z - \omega_0 t)$ representation, a linearly polarized electric field propagating along z direction can be written as

$$\mathbf{E}(z, t) = \hat{\mathbf{e}} A(z, t) \exp[i(k_0 z - \omega_0 t)], \quad (\text{A.7})$$

where $\hat{\mathbf{e}}$ is the unit vector of polarization of electric field, ω_0 the carrier frequency, k_0 the carrier wave number, and $A(z, t)$ the pulse envelope function. The form of $\mathbf{D}_L(z, t)$ becomes

$$\mathbf{D}_L(z, t) = \int_{-\infty}^{+\infty} n_0^2(\omega) \tilde{E}(z, \omega) \exp(-i\omega t) d\omega, \quad (\text{A.8})$$

where

$$\tilde{E}(z, \omega) = \frac{1}{2\pi} \int_{-\infty}^{+\infty} E(z, t) \exp(i\omega t) dt. \quad (\text{A.9})$$

If the $(\omega_0 t - k_0 z)$ representation is used, one obtains sign changes in the final reduced wave equation.

Using the foregoing equations, we can write the linear polarization term on the left-hand side of the one-dimensional wave equation as

$$\begin{aligned} & -\frac{1}{c^2} \frac{\partial^2}{\partial t^2} \mathbf{D}_L(z, t) \\ & = -\frac{1}{c^2} \int_{-\infty}^{+\infty} (-\omega^2) n_0^2(\omega) \tilde{E}(z, \omega) \exp(-i\omega t) d\omega \\ & = \frac{1}{2\pi} \int_{-\infty}^{\infty} \int_{-\infty}^{\infty} k^2(\omega) A(z, t') \exp[i\omega(t' - t)] \exp[i(k_0 z - \omega_0 t')] d\omega dt'. \quad (\text{A.10}) \end{aligned}$$

The derivation of the wave equation then proceeds by expanding $k^2(\omega)$ about the carrier frequency ω_0 in the form:

$$k^2(\omega) \approx k_0^2 + 2k_0 k_0^{(1)}(\omega - \omega_0) + k_0 k_p^{(2)}(\omega - \omega_0)^2 + \dots, \quad (\text{A.11})$$

where $k_0 = k(\omega_0)$ is the propagation constant, $k_0^{(1)} = \left. \frac{\partial k}{\partial \omega} \right|_{\omega=\omega_0}$ is the inverse of group velocity, and $k_0^{(2)} = \left. \frac{\partial^2 k}{\partial \omega^2} \right|_{\omega=\omega_0}$ is the inverse of group velocity of dispersion. It is then possible to evaluate the integral of Eq. (A.10) by using the convenient delta function identities

$$\frac{1}{2\pi} \int_{-\infty}^{\infty} \exp[i(\omega - \omega_0)(t' - t)] d\omega = \delta(t' - t) \quad (\text{A.12})$$

as well as

$$\frac{1}{2\pi} \int_{-\infty}^{\infty} (\omega - \omega_0) \exp[i(\omega - \omega_0)(t' - t)] d\omega = i\delta^{(1)}(t' - t), \quad (\text{A.13})$$

and

$$\frac{1}{2\pi} \int_{-\infty}^{\infty} (\omega - \omega_0)^2 \exp[i(\omega - \omega_0)(t' - t)] d\omega = -\delta^{(2)}(t' - t). \quad (\text{A.14})$$

In these relations, $\delta^{(n)}(t)$ is an n th-order derivative of the Dirac delta function, with the property that

$$\int_{-\infty}^{\infty} \delta^{(n)}(t - t_0) f(t) dt = \left. \frac{d^n f(t)}{dt^n} \right|_{t=t_0} \quad (\text{A.15})$$

when applied to a function $f(t)$. Substitute Eq. (A.11) into Eq. (A.10) and use Eq. (A.12) to (A.15), the second term on the left-hand side of Eq. (1.5) becomes

$$\begin{aligned}
& -\frac{1}{c^2} \frac{\partial^2}{\partial t^2} \mathbf{D}_L(z, t) \\
& = \frac{1}{2\pi} \int_{-\infty}^{\infty} \int_{-\infty}^{\infty} \left[k_0^2 + 2k_0 k_0^{(1)} (\omega - \omega_0) + k_0 k_0^{(2)} (\omega - \omega_0)^2 \right] A(z, t') \\
& \quad \times \exp[i\omega(t' - t)] \exp[i(k_0 z - \omega_0 t)] d\omega dt' \\
& = \int_{-\infty}^{\infty} \left[k_0^2 \delta(t' - t) + i2k_0 k_0^{(1)} \delta^{(1)}(t' - t) - k_0 k_0^{(2)} \delta^{(2)}(t' - t) \right] A(z, t') \\
& \quad \times \exp[i(k_0 z - \omega_0 t)] dt' \\
& = \left[k_0^2 A + i2k_0 k_0^{(2)} \frac{\partial A}{\partial t} - k_0 k_0^{(2)} \frac{\partial^2 A}{\partial t^2} \right] \exp[i(k_0 z - \omega_0 t)]. \tag{A.16}
\end{aligned}$$

Neglecting the second derivative of $A(z, t)$ with respect to z and $\frac{\partial^2}{\partial t^2} |A(z, t)|^2$. $A(z, t)$, the first term on the left-hand side and the term on the right-hand side of Eq. (1.5) are simply

$$\frac{\partial^2 E(z, t)}{\partial z^2} \approx \left[-k_0^2 A(z, t) + i2k_0 \frac{\partial A(z, t)}{\partial z} \right] \exp[i(k_0 z - \omega_0 t)], \tag{A.17}$$

and

$$\frac{2n_0 \bar{n}_2}{c^2} \frac{\partial^2}{\partial t^2} |E|^2 E \approx -\frac{n_0 n_2 \omega_0^2}{c^2} |A|^2 A \exp[i(k_0 z - \omega_0 t)], \tag{A.18}$$

respectively.

Inserting Eqs. (A.16) to (A.18) into Eq. (1.5), the wave equation for electric field reduces to the wave equation for the pulse envelope

$$i \left(\frac{\partial A}{\partial z} + \frac{1}{v_g} \frac{\partial A}{\partial t} \right) - \frac{1}{2} k_0^{(2)} \frac{\partial^2 A}{\partial t^2} + \frac{\omega_0}{2c} n_2 |A|^2 A = 0, \tag{A.19}$$

where $v_g \equiv 1/k_0^{(1)}$ is the group velocity. In Eq. (A.19), the first two terms describe the envelope propagation at the group velocity v_g ; the third term determines the temporal pulse broadening due to group velocity dispersion; the fourth characterizes the second order of the nonlinear polarization, which is responsible for the self-phase modulation effect and spectral broadening. Neglecting the group velocity dispersion term in Eq. (A.19), we obtain

$$\frac{\partial A}{\partial z} + \frac{1}{v_g} \frac{\partial A}{\partial t} = i \frac{\omega_0}{2c} n_2 |A|^2 A. \tag{A.20}$$

This is Eq. (2.2).

The Supercontinuum Laser Source
Fundamentals with Updated References

Alfano, R.R. (Ed.)

2006, XXII, 538 p. 259 illus.,

ISBN: 978-0-387-25097-7